Abstract

HEHR, BRIAN DOUGLAS. High Temperature Graphite Simulations using Molecular Dynamics. (Under the direction of Ayman I. Hawari).

Graphite, a major structural and moderator material in the proposed Generation IV reactor roadmap, is expected to experience irradiation at temperatures up to 1800 K. In this study, molecular dynamics (MD) is employed to investigate the physical properties of graphite from 0 K to 1800 K. MD applies the classical laws of physics to simulate atomistic-level behavior, and from the observed microscopic data, macroscopic properties may be surmised.

For the purposes of this study, a graphite-specific MD code was created and benchmarked against high temperature graphite data. Modifications were introduced into the interatomic potential function as needed to fit experimental measurements. Graphite-specific modifications include a plane-by-plane center of mass velocity correction, an additional potential energy cutoff function for out-of-plane displacements, and temperature-dependent parameterization of the potential function. These adjustments were fitted to high temperature measurements of thermal expansion and mean squared displacement.

The refined MD model of graphite was subsequently utilized to examine the threshold displacement energy at temperatures ranging from 300 K to 1800 K. It was found that the threshold energy depends strongly on the knock-on direction, as is expected due to the highly anisotropic nature of graphite. MD calculations of the threshold energy exhibited good agreement with the results of two electron irradiation studies.

High Temperature Graphite Simulations Using Molecular Dynamics

by

Brian D. Hehr

A thesis submitted to the Graduate Faculty of North Carolina State University in partial fulfillment of the requirements for the Degree of Master of Science

Nuclear Engineering

Raleigh, NC

2007

Approved by:

_____	_____
Dr. Bernard W. Wehring	Dr. K. L. Murty

_____

Dr. Ayman I. Hawari,
Chair of Advisory Committee

Biography

Brian Douglas Hehr was born in Reading, Pennsylvania on December 21, 1981 to parents Steven and Brenda Hehr. At the age of 3, Brian and his family moved to the vicinity of Charlotte, NC. Brian graduated from Sun Valley High School in 2000 and subsequently enrolled at North Carolina State University, where he graduated *summa cum laude* with dual B.S. degrees in physics and nuclear engineering. During his undergraduate studies, Brian participated in four summer internships – two at the Clariant Corporation headquarters in Charlotte and two at Los Alamos National Laboratory in New Mexico.

Immediately following graduation, Brian began working with Dr. Ayman Hawari of North Carolina State University on atomistic graphite simulations. During his first year of graduate study, Brian traveled to Tokyo to marry his long-time pen pal Atsuko Miyamoto, who has since become a permanent resident of the U.S.

Acknowledgements

I would like to offer my gratitude to Dr. Ayman Hawari, who originated the ideas behind this project and guided its subsequent development. I would additionally like to thank him for offering valuable input on papers and presentations that I composed during the course of my studies.

I would also like to extend my appreciation to Dr. Victor Gillette for setting aside many hours of his time to help guide me through the initial stages of the project, and for educating me about his homeland of Argentina.

Finally, I would like to recognize the Advanced Fuel Cycle Initiative of the US DOE Office of Nuclear Energy for their support via the AFCI / GNEP Fellowship Program. The University Research Alliance did a great job of administering fellowship funds diligently and responsively, and I'm very grateful for the opportunity afforded to me by the fellowship to visit Idaho National Laboratory and the DOE headquarters in Washington D.C. At both locations, I was highly impressed with the hospitality and enthusiasm of our hosts.

Table of Contents

List of Tables

List of Figures

Chapter 1
Introduction

1.1 Introduction

Graphite – in one form or another – has been a significant nuclear material ever since the inception of controlled fission in the 1930's and 40's. In fact, the world's first functional nuclear reactor (referred to as Chicago Pile-1) contained piles of graphite blocks that slowed neutrons down to the thermal energy range. Graphite-moderated reactors have subsequently been constructed in several nations for research or power generation purposes.

While light water reactors (LWRs) presently dominate the realm of commercial nuclear power production, graphite remains one of the foremost candidate materials for use in the proposed Generation IV reactor designs. Its attractiveness lies in an almost unique combination of desirable properties, including:

- High mechanical strength
- Large heat capacity
- Very high melting temperature
- Small cross section for neutron absorption
- Relatively low density

Despite the increasingly important role of graphite, its response to a high-temperature, irradiated environment has yet to be comprehensively investigated. To fill this need, the present work was undertaken with the purpose of developing a molecular dynamics code capable of simulating the physical behavior of graphite at high temperatures. This capability,

in conjunction with experimental studies, provides an excellent array of tools for examining the behavior of graphite in a Generation IV type environment.

1.2 Generation IV Concept and the VHTR

The Generation IV initiative is a global partnership that aims to deploy a new generation of safe, economical, sustainable, and reliable reactors for the purpose of commercial energy generation. Presently, the vast majority of commercial reactors are water cooled and moderated, with power production taking place in a network of UO_2 fuel assemblies. While these light water reactors (LWRs) have an excellent operating record, new advances have led to the conceptualization and initial design of several innovative reactor concepts, among which the Very High Temperature Reactor (VHTR) has figured prominently.

Like the LWR, the VHTR is envisioned as a thermal spectrum reactor in which low enriched uranium (LEU) comprises the primary fuel. The VHTR, however, would operate at a temperature of approximately 1000°C – much higher than the standard outlet temperature of an LWR. Furthermore, the VHTR is graphite moderated and helium cooled, leading to vastly different design considerations on the primary side of the system. A diagram of the proposed VHTR system is shown in Fig. 1-1. One effect of the higher operating temperature is to increase the efficiency of energy conversion; whereas most LWRs possess a conversion efficiency of well under 40%, the VHTR is predicted to achieve greater than 50% efficiency. An additional effect of the high outlet temperature – one that is, at present, unique to the

VHTR – is the potential coupling of the reactor system to an external thermochemical process for producing hydrogen gas, steel, or aluminum.

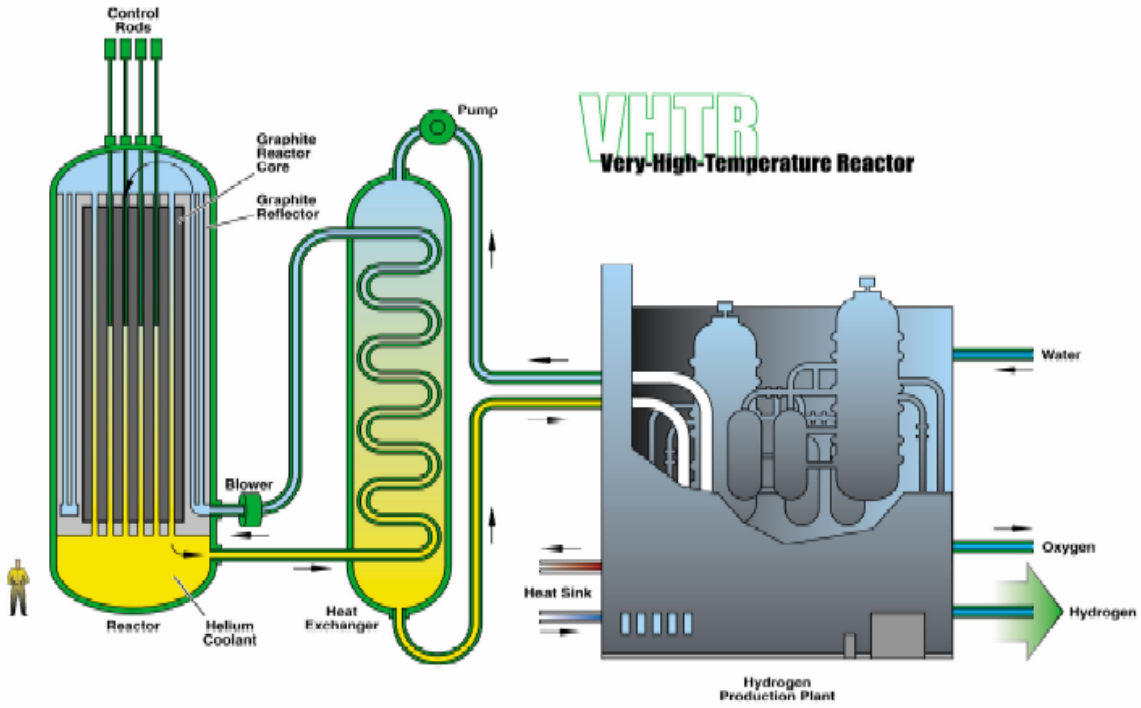

Fig. 1-1. Schematic of the proposed VHTR system including a coupled hydrogen production facility [1].

A number of factors lie behind the choice of graphite as the preferred moderator for the VHTR. First, in terms of the moderating figure of merit (FOM):

$$FOM = \frac{\Sigma_s \xi}{\Sigma_a} \tag{1.1}$$

graphite's FOM of 192 compares quite favorably against the FOM of 71 for light water. Here, Σ_s and Σ_a are the macroscopic scattering and absorption cross sections respectively and ξ is the average lethargy gain per collision. The superiority of graphite in this respect is mainly due to its relatively small absorption cross section for thermal neutrons. Being a solid

state moderator, graphite further performs the function of a structural material. This is made possible by its exceptionally high melting temperature of approximately 3700°C.

The static residence of graphite in the reactor core implies that radiation-induced defects will accumulate over time and may exert a significant impact of the properties of the moderator. In view of this fact, the present work focuses on the development of a high temperature molecular dynamics code for graphite and its application in performing an initial evaluation of defect formation at various temperatures between 300 K and 1800 K (up to the accident temperature of the VHTR).

1.3 Relevance to Thermal Neutron Scattering

In addition to the impact of neutron irradiation on the mechanical and physical properties of graphite, which is well documented in literature [2], there are reasons to believe that neutronic properties also can be affected. Because the introduction of vacancies and interstitials into the lattice structure perturbs the phonon frequency spectrum, the presence of these defects can impact neutron interactions in the thermal energy range – where phonon creation and annihilation processes contribute sizably to the scattering cross section [3]. The resulting change in the thermal neutron energy spectrum has implications in safety and criticality assessment of nuclear reactors.

As it turns out, the atomic trajectory data obtainable from a molecular dynamics simulation can straightforwardly be converted into the thermal scattering law, which is the fundamental input for calculating the differential scattering cross section of a material. Expressly, the differential scattering cross section may be written as [4]:

$$\frac{d^2\sigma}{d\Omega dE} = \frac{1}{4\pi}\frac{k'}{k}\left(\sigma_{cok} S\left(\vec{Q}, w\right) + \sigma_{incoh} S_s\left(\vec{Q}, w\right)\right) \tag{1.2}$$

where k and k' represent the magnitude of the wave vector of the incident and scattered neutron respectively, σ_{coh} is the bound atom coherent scattering cross section, σ_{incoh} is the bound atom incoherent scattering cross section, and $S\left(\vec{Q}, w\right)$ is the scattering law in which $\vec{Q} = \vec{k} - \vec{k}'$. The scattering law may be decomposed into two terms:

$$S\left(\vec{Q}, w\right) = S_s\left(\vec{Q}, w\right) + S_d\left(\vec{Q}, w\right) \tag{1.3}$$

where S_s is the self scattering law and S_d is the distinct scattering law. Of these two functions, the self scattering law is typically much simpler to calculate. Thus, the primary challenge lies in determining the distinct component or, alternatively, the total scattering law, from which S_d can be extracted via Eq. (1.3). Using the Van Hove formulation, the total scattering law may be written as:

$$S\left(\vec{Q}, w\right) = \frac{1}{2\pi\hbar}\int_{-\infty}^{\infty}\int_{-\infty}^{\infty} G\left(\vec{r}, t\right) e^{i\left(\vec{Q}\cdot\vec{r} - wt\right)} d\vec{r}\, dt \tag{1.4}$$

in which $G\left(\vec{r}, t\right)$ is the probability of finding the atom at position $\vec{r}$ at time t. Since the atomic positions are known exactly throughout the time evolution of an MD system, $G\left(\vec{r}, t\right)$ is directly calculable in MD and the scattering law may be computed by taking the Fourier transform of $G\left(\vec{r}, t\right)$ as in Eq. (1.4). This approach applies to both damaged and undamaged systems.

1.4 Structure of Graphite

Fig. 1-2 illustrates the structure of graphite – a semi-metallic allotrope of carbon. Graphite features hexagonal ABAB stacking with an interplanar gap that is sufficiently large

to permit only Van der Waals interactions between atoms occupying different planes. Very strong covalent bonds exist within each plane, and the exceptionally large cohesive energy of 7.37 eV is primarily responsible for the high melting temperature of graphite. Conductivity is also dependent on crystallographic direction, with a high in-plane conductivity arising from the presence of de-localized electrons. These electrons are further responsible for graphite's dull, metallic appearance, shown in Fig. 1-3.

The layered atomic arrangement inherent in graphite also produces strong anisotropy in properties such as thermal expansion. For this reason, nuclear-grade graphite is usually fabricated with randomly orientated grains such that the randomness of the aggregate effectively averages out the anisotropic behavior of the pyrolytic variety, generating an isotropy that is conducive to core stability. Nuclear graphite must also be free of neutron absorbing impurities, particularly boron.

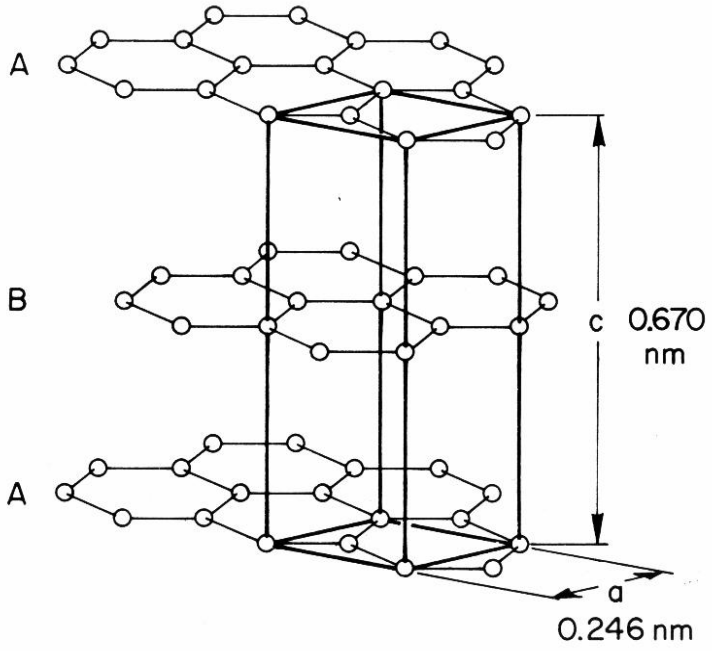

Fig. 1-2 The crystal structure of perfect graphite, with the unit cell demarcated in bold lines. Also shown are the characteristic lattice parameters at 0 K.

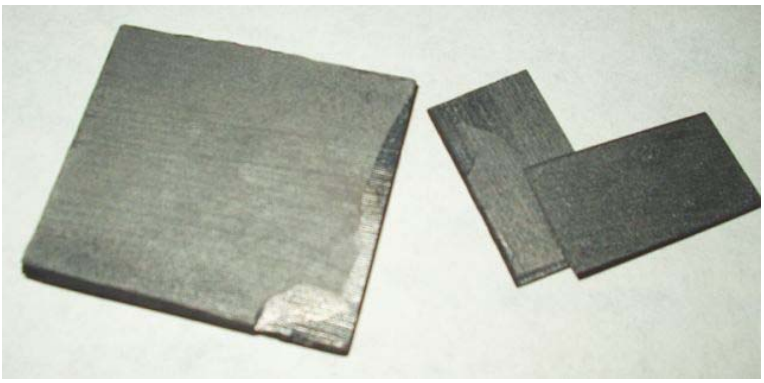

Fig. 1-3 Sheets of pyrolytic graphite

1.5 Computational Techniques

Lattice dynamics and molecular dynamics (MD) are the main techniques for simulating material behavior on the atomistic level. These two methods differ in that lattice dynamics typically consigns atoms to discrete lattice points, whereas no such restriction is enforced within a molecular dynamics simulation. In either case, interatomic interactions may be evaluated using either an empirical or an ab-initio ("first principles") potential energy function. The latter refers to a simplified quantum mechanical structure calculation while the former involves fitting a user-defined potential function to material properties. However, the empirical approach is not completely detached from quantum mechanics, because the chosen forms of the empirical formulae are often based on quantum mechanical models.

While the empirical approach clearly limits the transferability of the derived potential function, it typically allows for much greater computational efficiency, thereby placing less severe restrictions on the size and/or time scale of the simulated system. Because this work encompasses damaged structures as well as high temperature dynamics on the picosecond

scale, the empirical molecular dynamics technique was selected as the appropriate methodology. The remainder of this discussion shall therefore focus on empirical MD.

1.6 History of MD

While the first MD simulations of realistic systems emerged as recently as the 1960's and 70's, the foundational concepts of MD stretch far back into antiquity [5]. In fact, much of modern physics – most conspicuously, quantum theory – is left unaddressed in the realm of MD, in which Newton's equations of motion form the primary theoretical underpinning. By treating atoms as point masses, MD bypasses a direct handling of the electronic interactions that place such a high computational cost on *ab initio* calculations. The price of these simplifications takes the form of two fundamental approximations:

1. That the modeled system may be accurately represented using only the classical laws of physics (with the possible inclusion of semiclassical corrections)
2. That interatomic interaction may be reduced to a potential energy function comprised of two- and/or three-body terms.

Despite the seeming restrictiveness of the above approximations, MD has proven remarkably useful for computational investigations of a wide range of substances in the liquid, solid, and gaseous phases. From early studies of the phase diagram of argon to recent, large-scale studies of highly complex systems such as the complete satellite tobacco mosaic virus, MD has met with considerable success in diverse endeavors.

Chapter 2

Basics of Molecular Dynamics

2.1 Introduction

Molecular dynamics (MD) is a simulation technique in which an interacting atomic system is allowed to evolve for a specified period of time under the laws of classical physics. MD derives its simplicity and relatively low computational cost from the assumption that atomic trajectories may be evaluated via Newton's 2nd law, which can be written as follows:

$$\vec{F}_i = -\nabla_{r_i} V = m_i \frac{d^2 \vec{r}_i}{dt^2} \tag{2.1}$$

where V is the potential energy of the system, $\vec{r}_i$ is the position vector of atom i, m_i is the mass of atom i, and t is time. In practice, MD simulations must progress in accordance with a finite time step, and so the standard methodology is to implement Eq. (2.1) using finite difference techniques.

2.2 Finite Difference Method

The finite difference scheme employed to solve Eq. (2.1) is the heart of any MD simulation, and in order to function well, the truncation error of the chosen scheme must be low enough to allow for a sufficiently large time step. Otherwise, more steps will be needed to simulate a given length of time. The computational efficiency of the algorithm should also be as high as possible, but truncation error is usually the foremost issue. This is because the force calculation is almost always the most costly part of an MD program, and the number of force calculations is directly proportional to the number of time steps.

Several methods of finite difference evaluation are in common usage (e.g. the leapfrog, Verlet, and predictor-corrector methods). Each of these algorithms begins with a Taylor expansion about the atomic positions [6]:

$$\vec{r}(t+\Delta t) = \vec{r}(t) + \frac{d\vec{r}(t)}{dt}[\Delta t] + \frac{1}{2}\frac{d^2\vec{r}(t)}{dt^2}[\Delta t]^2 + \frac{1}{6}\frac{d^3\vec{r}(t)}{dt^3}[\Delta t]^3 + \ldots \tag{2.2}$$

$$= \vec{r}(t) + \vec{v}(t)[\Delta t] + \frac{1}{2}\vec{a}(t)[\Delta t]^2 + \frac{1}{6}\vec{b}(t)[\Delta t]^3 + \ldots \tag{2.3}$$

Similarly,

$$\vec{v}(t+\Delta t) = \vec{v}(t) + \vec{a}(t)[\Delta t] + \frac{1}{2}\vec{b}(t)[\Delta t]^2 + \ldots \tag{2.4}$$

$$\vec{a}(t+\Delta t) = \vec{a}(t) + \vec{b}(t)[\Delta t] + \ldots \tag{2.5}$$

where $\vec{v}$ is velocity, $\vec{a}$ is acceleration, and $\vec{b}$ is impulse. The remainder of this discussion will focus on the predictor-corrector method, which was implemented in the NCSU MD code for graphite.

2.3 Predictor-Corrector

From Eqs. (2.2) - (2.5), the particle positions and associated derivatives at time (t+Δt) may be estimated from quantities available at time (t). These estimations correspond to the "predictor" step of the algorithm. The predicted positions and accelerations shall be labeled $\vec{r}^{\,p}(t+\Delta t)$ and $\vec{a}^{\,p}(t+\Delta t)$ respectively, and similar notation is used for other derivatives of position. In matrix format, the predicted quantities are given by:

$$\begin{pmatrix} \vec{r}^{\,p}(t+\Delta t) \\ \vec{v}^{\,p}(t+\Delta t) \\ \vec{a}^{\,p}(t+\Delta t) \\ \vec{b}^{\,p}(t+\Delta t) \end{pmatrix} = \begin{pmatrix} 1 & 1 & 1 & 1 \\ 0 & 1 & 2 & 3 \\ 0 & 0 & 1 & 3 \\ 0 & 0 & 0 & 1 \end{pmatrix} \begin{pmatrix} \vec{r}_0(t) \\ \vec{r}_1(t) \\ \vec{r}_2(t) \\ \vec{r}_3(t) \end{pmatrix} \tag{2.6}$$

where $\vec{r}_0 = \vec{r}(t)$, $\vec{r}_1 = \frac{d\vec{r}(t)}{dt}[\Delta t]$, $\vec{r}_2 = \frac{1}{2}\frac{d^2\vec{r}(t)}{dt^2}[\Delta t]^2$, and $\vec{r}_3 = \frac{1}{6}\frac{d^3\vec{r}(t)}{dt^3}[\Delta t]^3$ correspond to the components of the Taylor expansion as shown on the RHS of Eq. (2.2).

After incrementing the particle positions in accordance with the predictor equations, the true accelerations are obtainable at $\{\vec{r}^{\,p}(t+\Delta t)\}$ via direct calculation of interatomic forces. The difference between the predicted and true accelerations constitutes an error signal of the form:

$$\Delta\vec{a}(t+\Delta t) = \vec{a}^{\,t}(t+\Delta t) - \vec{a}^{\,p}(t+\Delta t) \tag{2.7}$$

and the final, corrected trajectories are then given by:

$$\begin{pmatrix} \vec{r}^{\,c}(t+\Delta t) \\ \vec{v}^{\,c}(t+\Delta t) \\ \vec{a}^{\,c}(t+\Delta t) \\ \vec{b}^{\,c}(t+\Delta t) \end{pmatrix} = \begin{pmatrix} \vec{r}^{\,p}(t+\Delta t) \\ \vec{v}^{\,p}(t+\Delta t) \\ \vec{a}^{\,p}(t+\Delta t) \\ \vec{b}^{\,p}(t+\Delta t) \end{pmatrix} + \begin{pmatrix} c_0 \\ c_1 \\ c_2 \\ c_3 \end{pmatrix} \Delta\vec{a}(t+\Delta t) \tag{2.8}$$

Gear [7] has prescribed values for the coefficients $\{c\}$ that optimize the stability and accuracy of the predictor-corrector scheme. The optimized coefficients for a 2nd order differential equation of the form $\left(\frac{d^2r}{dt^2}\right) = f(r)$ are tabulated in Table 2.1. In the NCSU MD code, the Taylor expansion of Eq. (2.2) is truncated after the fourth term, and so the appropriate Gear coefficients correspond to the second line of Table 2.1.

Table 2.1. Gear coefficients for a 2nd order equation [6]

# expansion terms	c_0	c_1	c_2	c_3	c_4	c_5
3	0	1	1			
4	1/6	5/6	1	1/3		
5	19/120	3/4	1	1/2	1/12	
6	3/20	251/360	1	11/18	1/6	1/60

2.4 Periodic Boundary Conditions

The simulated atomic structure is customarily constructed by combining an integer number of crystallographic unit cells into a larger entity called the "supercell". Depending on the purpose of the simulation as well as the lattice type of the material, the user may find it desirable to create a non-uniform supercell that is skewed along a particular Cartesian axis. Yet, regardless of how the supercell is defined, a question arises regarding how to treat the boundary atoms if surface effects are not desired in the calculation.

One could simply construct a supercell of sufficient size to render surface effects negligible around the center of the cell. However, this approach is highly inefficient when compared to the technique of *periodic boundary conditions* (PBC).

The basic idea of PBC is to surround the supercell with identical images of itself such that atoms in the vicinity of the supercell border will "see" virtual atoms rather than empty space. Although these virtual atoms participate in interatomic force calculations, they are not moved independently via Newton's 2nd law nor are they included in system-wide averages. At all times, they merely mirror the movements of their supercell counterparts. Imposing PBC on a 3D supercell will bring about 26 images such that every face, edge, and corner of the supercell boundary is completely surrounded by the simulated crystal structure. The concept of PBC is illustrated in Fig. 2-1.

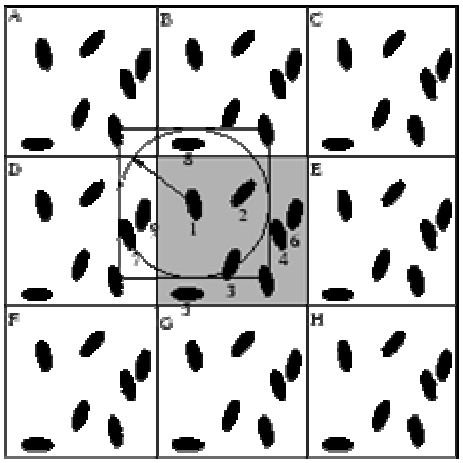

Fig. 2-1. Periodic Boundary Conditions. Cells A-H are images of the supercell. The interatomic interaction range must be less than the width of the supercell in order to prevent interaction between an atom and one of its images. [8]

An additional effect of PBC – shown in Fig. 2-2 – is that an atom exiting the supercell volume will instantly re-enter the supercell at another position. In other words, the exiting particle is replaced by one of its images so that the total number of atoms within the supercell is preserved.

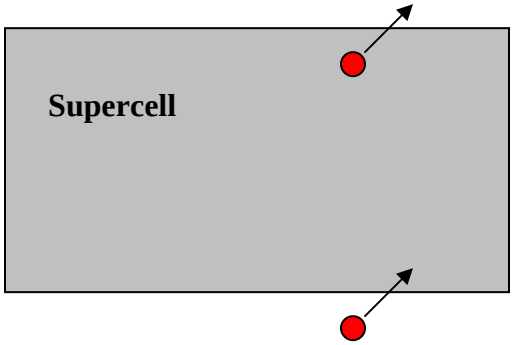

Fig. 2-2. Transport phenomenon under PBC. The particle exits from the upper-righthand corner and its image enters from the lower-righthand corner.

2.5 Ensembles

The concept of particle ensembles originates in statistical mechanics and is vital for attaining a theoretical understanding of the equilibrium state of an atomistic system. Fundamentally, ensemble theory endeavors to establish a connection between the microscopic traits of the system and macroscopically observable thermodynamic quantities. The word "ensemble" refers to the aggregate of possible configurations of a system that satisfy a given set of macroscopic constraints. Ensembles are commonly identified by these constraints; for example, the NVT ensemble is associated with a constant particle number, volume, and temperature.

In computational MD simulations, microscopic characteristics of the system (i.e. the positions, momenta, and particle interaction rules) are explicitly calculated or specified by the user, and quantities of interest (such as macroscopic observables) are generally computed as averages over the available microscopic data. Thus, the details of ensemble theory are not required to perform, or extract results from, a computational MD simulation. Indeed, ensemble theory deals only with the configurations of the system in position-momentum space and does not address its time evolution. The equivalence of time averaging and ensemble averaging is established by the *Ergodic hypothesis*, which, along with ensemble theory, is given a more detailed treatment in Appendix A.

2.6 Initial Velocities

The initial velocity components of each atom along the x, y, and z axes are typically determined through a random number generation scheme. Two physically important conditions should be enforced in setting the initial velocities:

$$\langle mv_x \rangle = \langle mv_y \rangle = \langle mv_z \rangle = 0 \tag{2.9}$$

$$\langle v_x^2 \rangle = \langle v_y^2 \rangle = \langle v_z^2 \rangle = \frac{k_B T}{m} \tag{2.10}$$

where v_x, v_y, and v_z are the x, y, and z components of velocity, m is the atomic mass, and k_B is Boltzmann's constant. Eq. (2.9) relates to the symmetric distribution of momenta about $\vec{p} = 0$ while Eq. (2.10) pertains to the equipartitioning of energy. The significance and implementation of Eq. (2.9) is discussed in the following section.

According to the equipartition theorem, an average energy of $\frac{1}{2}kT$ is associated with every independent degree of freedom of a molecule in thermal equilibrium. This provision is imposed in MD by scaling the initial random velocities by a uniform constant such that Eq. (2.10) is satisfied. Eqs. (2.9) and (2.10) together define an initial condition that facilitates meaningful investigation of the physical properties of the system.

2.7 Center of Mass Correction

As mentioned in the previous section, initialization of an MD simulation typically involves some degree of randomization in the initial velocities of the particles. In almost all cases, the center of mass velocity of the system will assume a small but nonzero value. This scenario is undesirable in standard MD simulations because the kinetic energy will consequently be shared between internal energy and bulk translational motion, causing difficulty to arise in correlating physical properties with temperature. To address this issue, most MD codes include a center of mass (CM) correction routine that first calculates the CM velocity via:

$$v_{cm} = \frac{\sum_j m_j \vec{v}_j}{\sum_j m_j} \tag{2.11}$$

and then scales the CM velocity to zero:

$$\vec{v}_j \rightarrow \vec{v}_j - \vec{v}_{cm} \qquad \text{for all atoms } j \tag{2.12}$$

Eq. (2.12) functions effectively when applied to isotropic materials; however, in the case of graphite, the weakness of the interplanar forces necessitates consideration of each plane as a distinct subsystem to which Eqs. (2.11) and (2.12) are applied on a plane-by-plane basis.

2.8 Velocity Rescaling

Temperature drifts arise naturally during the course of an MD simulation; this is because interatomic interactions follow Newton's 2nd law, which only guarantees conservation of total energy (i.e. the sum of kinetic and potential energy). Therefore, in generating a constant temperature ensemble, an additional algorithm is often needed to regulate the average kinetic energy from one time step to the next. The simplest method, velocity rescaling, is described below. Other possibilities are mentioned in Appendix A.

Classically, temperature can be related to kinetic energy via:

$$\frac{3}{2} k_B T = \langle KE \rangle = \left\langle \frac{1}{2} m v^2 \right\rangle \tag{2.13}$$

where KE is kinetic energy. Manipulating this equation yields an expression for temperature:

$$T = \frac{\langle m v^2 \rangle}{3 k_B} \tag{2.14}$$

which is easily calculable given the momenta of the particles. In general, the temperature computed using Eq. (2.14) will fluctuate during the course of an MD simulation. The simplest way to restore the desired temperature is to introduce a velocity scaling factor of the form:

$$F = \sqrt{\frac{T_o}{T_{actual}}} \tag{2.15}$$

where T_o is the desired temperature and T_{actual} is the temperature calculated from Eq. (2.14). This factor is applied to all particle velocities:

$$v_j \rightarrow F v_j \qquad \text{for all atoms } j \tag{2.16}$$

resulting in the correct average over kinetic energy.

2.9 Potential Energy Function

While many of the MD techniques so far discussed may be applied to a wide variety of systems, the potential energy function is highly material-dependent. This is partly due to the empirical nature of MD potentials. Instead of utilizing the more universal principles of quantum mechanics, empirical potentials treat the atoms as point masses that interact in a manner describable by relatively simple functions of the atomic positions. The point mass approximation is normally justified at temperatures above the Debye temperature of the material.

In general, the energy of a system of interacting particles may be written [9]:

$$U = \sum_i V_1(\vec{r}_i) + \sum_i \sum_{i<j} V_2(\vec{r}_i, \vec{r}_j) + \sum_i \sum_{i<j} \sum_{i<j<k} V_3(\vec{r}_i, \vec{r}_j, \vec{r}_k) + \ldots \tag{2.17}$$

where the potential function, U, is labeled an "m-body" potential when the RHS is expanded up to V_m. The reactive bond order (REBO) potential, which applies Eq. (2.17) to hydrocarbons specifically, will be examined in detail. First, the origin of the REBO potential will be elucidated through discussion of the Abell formalism – a precursor to the class of bond order potentials of which REBO is a member.

2.9.1 Abell Formalism

The formalism introduced by Abell [10] was foundational to the subsequent bond order schemes refined by Tersoff [9] and Brenner [11]. Starting from the quantum mechanical equations that describe molecular binding, Abell demonstrated that the interatomic binding energy could be expressed as:

$$E = \sum_k Z_k \left(q V_{Rk} + p_k V_{Ak} \right) \tag{2.18}$$

where E is the binding energy per atom, Z_k is the number of atoms in the k^{th}-neighbor coordination shell, p_k is the bond order term, q is the number of valence electrons per atom, and V_{Ak} and V_{Rk} are functions describing interatomic attraction and repulsion respectively. In all cases, the k subscript refers to the k^{th} coordination shell relative to some reference atom. It should be emphasized that the summation of Eq. (2.18) is not restricted to nearest neighbors of the reference atom and, in principle, includes all atoms of the system.

Nearest Neighbor Approximation

To validate the simplification of Eq. (2.18) to include only nearest neighbors, Abell states the following arguments:

1. The repulsive term, V_{Rk} – which includes the Pauli overlap repulsion and electrostatic repulsion – falls off much more rapidly than V_{Ak} and may be cut off beyond the first coordinate shell.
2. To a very good approximation,

$$\sum_k Z_k \upsilon_k p_k \cong Zp$$

where $\upsilon_k = \frac{V_{Ak}}{V_{A1}}$ is the ratio of the attractive term of the k^{th} shell to that of the 1^{st} shell.

3. Even when V_{Ak} decays slowly with distance, the effect of interactions beyond the first shell may be treated as a small perturbation.

The third argument is posited without elaboration and is effectively an assumption. Abell adopts the second argument as the primary justification for the nearest neighbor approximation. Overall, it is evident that this approximation lacks rigorous reinforcement and certainly does not hold for all materials (particularly simple metals). Indeed, validation of the nearest neighbor approximation is chiefly *a posteriori* in that numerous studies have since demonstrated its capacity to agree with the observed properties of a wide range of materials.

Attractive and Repulsive Terms

Under the nearest neighbor approximation, Eq. (2.18) becomes:

$$E = Z\left[qV_R(r) + pV_A(r)\right] \tag{2.19}$$

where *r* is the interatomic distance. To make this formula more explicit, functional forms for V_R and V_A must be specified. Abell selects the following representations:

$$V_R = A\exp(-\Theta r) \tag{2.20}$$

$$V_A = -B\exp(-\lambda r) \tag{2.21}$$

in which A,B, Θ, and λ are positive definite quantities characteristic of the given atomic species. Considerable support exists for the exponential form, namely that:

1. Atomic orbitals decay exponentially with *r*
2. Diatomic potentials have often been represented exponentially, as have pair interactions in transition metals and semiconductors.
3. *Ab initio* calculations of hydrogen and lithium show a nearly exponential decay with *r*.

Bond Order

With the form of V_A and V_R defined explicitly, the principal remaining task is to represent the bond order, p, in terms of physical quantities. Abell shows that, for a Bethe lattice, the bond order may be expressed as:

$$p_\beta(Z,q) = -\frac{1}{Z}\int_{-\infty}^{\varepsilon_F} \varepsilon n_\beta(Z,\varepsilon)d\varepsilon \tag{2.22}$$

where ε is energy, ε_F is the Fermi level, and n_β, the density of states per site for a Bethe lattice, is given by:

$$\pi n_\beta(Z,\varepsilon) = \theta\left(4[Z-1]-\varepsilon^2\right)\cdot\frac{Z\sqrt{\left(4[Z-1]-\varepsilon^2\right)}}{\left(Z^2-\varepsilon^2\right)} \tag{2.23}$$

in which θ denotes the unit step function. Applying a large-Z expansion to the density of states allows for Eq. (2.22) to be evaluated analytically, and the first-order result is:

$$p_\beta(Z,q) \cong \alpha(q)\frac{1}{\sqrt{Z}} \tag{2.24}$$

which indicates that the bond order is inversely proportional to the square root of the coordination number.

2.9.2 Reactive Bond Order Potential (REBO)

Elaborating upon the basic ideas expounded by Abell and Tersoff, Brenner [11] created a similar potential aimed at modeling hydrocarbons. In addition to re-parameterizing the Tersoff formulation, this 1st generation REBO potential augmented the bond order term with an explicit function of coordination number.

Publication of the 2nd generation REBO potential [12] marked the latest landmark in this family of potentials. While retaining the basic equation for binding energy used by Abell and Tersoff, Brenner and coworkers increased the sophistication of the pairwise attractive and repulsive functions in order to simultaneously fit the bond lengths, cohesive energies, and force constants of several carbon-carbon and carbon-hydrogen structures. Moreover, the size of the fitting library was expanded, and a torsional term was added to the bond order.

The 2nd generation REBO potential will now be discussed in detail. The total binding energy is given by:

$$E = \sum_i \sum_{j>i} f_C(r_{ij})\left[V_R(r_{ij}) + \bar{b}_{ij} V_A(r_{ij})\right] \tag{2.25}$$

where V_R and V_A are pairwise repulsive and attractive functions, $\bar{b}_{ij}$ is the bond order term, r_{ij} is the distance between atoms *i* and *j*, and $f_C(r_{ij})$ is a cutoff function that smoothly tapers the potential energy to zero starting at some specified distance beyond the 1st coordination shell.

Cutoff Function

The cutoff function, which enforces the nearest-neighbor approximation proposed by Abell, is written as:

$$f_c(r_{ij}) = \begin{cases} 1 & , r_{ij} < R_{in} \\ \frac{1}{2}\left\{1+\cos\left[\pi\frac{(r_{ij}-R_{in})}{(R_{out}-R_{in})}\right]\right\} & , R_{in} < r_{ij} < R_{out} \\ 0 & , r_{ij} > R_{out} \end{cases} \quad (2.26)$$

in which R_{in} and R_{out} (i.e. the inner and outer cutoffs) are the interatomic distances at which the sinusoidal cutoff begins and ends. In REBO, R_{in} and R_{out} are set to 1.7 Å and 2.0 Å respectively. This is acceptable for graphite, in which the 1st neighbor distance of 1.42 Å falls well within the inner cutoff range and the 2nd neighbor distance of 2.46 Å is well beyond the outer cutoff limit, meaning that the potential energy calculation is indeed restricted to nearest neighbors.

Attractive and Repulsive Functions

The pairwise repulsive and attractive functions are given as follows:

$$V^R = \left(1+\frac{Q}{r_{ij}}\right)A\exp(-\alpha r_{ij}) \quad (2.27)$$

$$V^A = \sum_{n=1,3} B_n \exp\left(-\beta_n r_{ij}\right) \tag{2.28}$$

where A, Q, α, B_n, and β_n are fitting constants. The $\left(Q / r_{ij}\right)$ term prevents atoms from approaching each other too closely during energetic collisions. The rationale behind the exponential dependence on r_{ij} was discussed in section 2.9.1.

Bond Order

The bond order term consists of four distinct components:

$$\bar{b}_{ij} = \frac{1}{2}\left[b_{ij}^{\sigma-\pi} + b_{ji}^{\sigma-\pi}\right] + \Pi_{ij}^{RC} + b_{ij}^{DH} \tag{2.29}$$

in which $b_{ij}^{\sigma-\pi}$ depends on local coordination and bond angle as follows:

$$b_{ij}^{\sigma-\pi} = \left[1 + \sum_{k\neq(i,j)} f_{ik}^c\left(r_{ik}\right)\cdot g_c e^{\lambda_{ijk}} + P_{ij}\left(N_i^C, N_i^H\right)\right]^{-0.5} \tag{2.30}$$

where g_c is a function of the angle between the i-j and i-k bond. For graphite, λ_{ijk} and P_{ij} are zero. The term N_i^C refers to the number of carbon atoms surrounding atom *i* (excluding the i-j bond) and can be expressed in terms of the cutoff function via:

$$N_i^c = \sum_{k(\neq i,j)} f_{ik}^c\left(r_{ik}\right) \tag{2.31}$$

which allows for fractional values if $R_{in} < r_{ik} < R_{out}$. It can be demonstrated that $b_{ij}^{\sigma-\pi}$ approaches the bond order expression derived by Abell (Eq. (2.24)) under the same large-Z approximation. To see this, Eq. (2.30) may be written (for graphite) as:

$$b_{ij}^{\sigma-\pi} = \left[1 + \sum_{k\neq(i,j)} f_{ik}^c\left(r_{ik}\right)\cdot g_c\right]^{-0.5} \tag{2.32}$$

And because:

$$\sum_{k(\neq i,j)} f_{ik}^{c}(r_{ik}) \propto Z \tag{2.33}$$

it is apparent that, for a large number of neighbors, the following holds:

$$b_{ij}^{\sigma-\pi} \cong \left[\sum_{k\neq(i,j)} f_{ik}^{c}(r_{ik}) \cdot g_c \right]^{-0.5} \propto \frac{1}{\sqrt{Z}} \tag{2.34}$$

which is exactly the proportionality derived by Abell.

Bond Angle Term

The angular function g_c is given by:

$$g_c = G_c(\cos\theta_{ijk}) + Q(N_i^t)\left[\gamma_c(\cos\theta_{ijk}) - G_c(\cos\theta_{ijk})\right] \tag{2.35}$$

where $G_c(\cos\theta_{ijk})$ and $\gamma_c(\cos\theta_{ijk})$ are 5th degree polynomial splines and θ_{ijk} is the angle between the i-j and i-k bond. The function $Q(N_i^t)$ discriminates between low and high coordination structures and is defined as:

$$Q_i(N_i^t) = \begin{cases} 1 & , N_i^t < 3.2 \\ \frac{1}{2}\left\{1+\cos\left[2\pi\left\{N_i^t - 3.2\right\}\right]\right\} & , 3.2 < N_i^t < 3.7 \\ 0 & , 3.7 < N_i^t \end{cases} \tag{2.36}$$

where $N_i^t = N_i^H + N_i^C$ is the total number of carbon and hydrogen atoms surrounding atom *i*. In the case of graphite, clearly $N_i^t = N_i^C$.

Conjugation Term

The function Π_{ij}, representing the impact of radical energetics and pi-bond conjugation, takes the form of a tricubic spline:

$$\Pi_{ij}^{RC} = F_{ij}\left(N_i^t, N_j^t, N_{ij}^{conj}\right) = \sum_{l=0}^{3}\sum_{m=0}^{3}\sum_{n=0}^{3} a_{lmn}^{\left(N_i^t, N_j^t, N_{ij}^{conj}\right)} \left(N_i^t\right)^l \left(N_j^t\right)^m \left(N_{ij}^{conj}\right)^n \tag{2.37}$$

in which a set of 64 constants a_{lmn} is fitted to each permutation of $\left(N_i^t, N_j^t, N_{ij}^{conj}\right)$ subject to the following rules:

$$F_{ij}\left(N_i^t, N_j^t, N_{ij}^{conj}\right) = F_{ij}\left(N_j^t, N_i^t, N_{ij}^{conj}\right) \tag{2.38}$$

$$F_{ij}\left(N_i^t > 3, N_j^t, N_{ij}^{conj}\right) = F_{ij}\left(3, N_j^t, N_{ij}^{conj}\right) \tag{2.39}$$

$$F_{ij}\left(N_i^t, N_j^t, N_{ij}^{conj} > 9\right) = F_{ij}\left(N_i^t, N_j^t, 9\right) \tag{2.40}$$

with N_{ij}^{conj} defined by:

$$N_{ij}^{conj} = 1 + \left[\sum_{k(\neq i,j)} f_{ik}^c\left(r_{ik}\right) F\left(x_{ik}\right)\right]^2 + \left[\sum_{l(\neq i,j)} f_{jl}^c\left(r_{jl}\right) F\left(x_{jl}\right)\right]^2 \tag{2.41}$$

where $F\left(x_{ik}\right)$ is given by:

$$F\left(x_{ik}\right) = \begin{cases} 1 & , x_{ik} < 2 \\ \frac{1}{2}\left\{1 + \cos\left[\pi\left\{x_{ik} - 2\right\}\right]\right\} & , 2 < x_{ik} < 3 \\ 0 & , x_{ik} > 3 \end{cases} \tag{2.42}$$

in which:

$$x_{ik} = N_k^t - f_{ik}^c\left(r_{ik}\right) \tag{2.43}$$

Within a perfect graphite system, $\left(N_i^t, N_j^t, N_{ij}^{conj}\right) = (2,2,9)$ for every i-j pair.

Torsional Term

Torsional effects are quantified through the expression:

$$b_{ij}^{DH} = T_{ij}\left(N_i^t, N_j^t, N_{ij}^{conj}\right)\left[\sum_{k(\neq i,j)}\sum_{l(\neq i,j)}\left(1 - \cos^2\left(\Theta_{ijkl}\right)\right) f_{ik}^c\left(r_{ik}\right) f_{jl}^c\left(r_{jl}\right)\right] \tag{2.44}$$

where the dihedral angle, Θ_{ijkl}, is calculated from $\hat{e}_{jik}$ and $\hat{e}_{ijl}$ -- unit vectors in the direction of $\left(\vec{r}_{ji} \times \vec{r}_{ik}\right)$ and $\left(\vec{r}_{ij} \times \vec{r}_{jl}\right)$ respectively -- as:

$$\cos\left(\Theta_{ijkl}\right) = \left(\hat{e}_{jik} \bullet \hat{e}_{ijl}\right) \tag{2.45}$$

and T_{ij} is a tricubic spline possessing the same form as Eq. (2.37) above but with a different set of fitted coefficients.

For graphite, application of the REBO potential at 0 K produces the potential energy curve shown in Fig. 2-3.

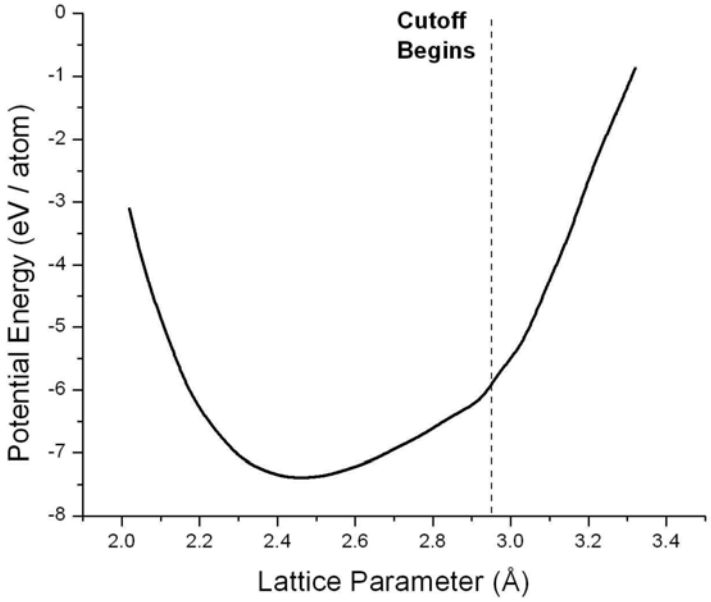

Fig. 2-3. The potential energy of graphite at 0 K vs. the in-plane lattice parameter, as computed using the REBO potential. At a lattice parameter of 2.94 Å, the 1st neighbor separation enters the cutoff range, causing a sudden increase in the potential energy gradient.

Chapter 3

Motivation for a New Model

3.1 Graphite Structure

While the REBO potential provides a fairly comprehensive treatment of short-range interactions, no attention is given to the long range forces that are vital to the stability of the graphite structure. The need for an additional component of the potential is illustrated in Fig. 3-1. These snapshots of the simulated atomic positions reveal that an entire plane of atoms may exhibit membrane-like vibrations unless a force is present to resist out-of-plane motion. The unnaturally large vibrations evident in Fig. 3-1 are also manifest in the out-of-plane mean squared displacement, displayed in Fig. 3-2.

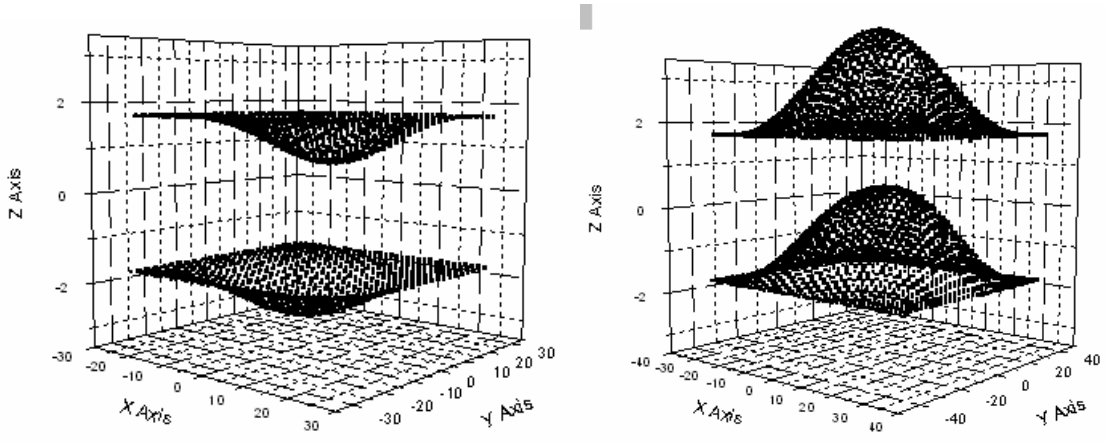

Fig. 3-1 The profile of a simulated array of graphite using the REBO potential with fixed boundary atoms. The atomic planes oscillate in an unphysical manner in the absence of long range forces.

Various researchers have introduced modified forms of REBO (e.g. the AIREBO potential [13]) that incorporate long range Van der Waals interactions. These efforts typically involve the addition of a Lennard-Jones type potential to the standard REBO formulation.

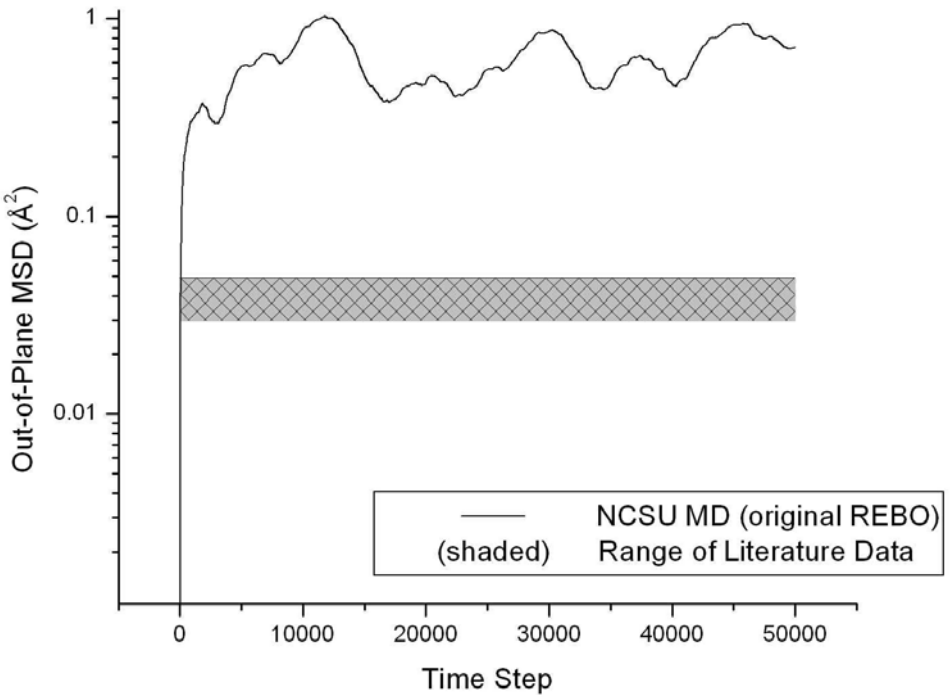

Fig. 3-2. The out-of-plane MSD at 1200 K as computed using the published form of REBO. The calculated MSD approaches equilibrium an order of magnitude above the band of MSD values reported in literature.

However, the explicit inclusion of long range interactions is computationally intensive, since the number of interacting pairs increases many fold. The approach taken in this work is to approximate long-range interactions using a function dependent only upon an atom's out-of-plane displacement relative to the interplanar spacing of the system (which, in turn, varies with temperature). This function is parameterized so as to fit experimental mean-squared displacement (MSD) data along the hexagonal c-axis.

3.2 Absolute Zero Fitting

Additional complications arise at high temperatures due to the manner in which the REBO potential is parameterized. As with the majority of empirical potential functions,

REBO employs a fitting database consisting only of absolute zero properties such as bond length, force constant, and atomization energy. Consequently, the fitted REBO constants are strictly suitable only at 0 K.

Combined with the general-purpose intent of REBO, this fact suggests that high temperature MD calculations will likely depart from experimental measurements. Indeed, such a discrepancy was found to exist in the thermal expansion coefficient. Fig. 3-3 illustrates the difference between MD and experiment. To improve the performance of REBO at high temperatures, a temperature-dependent adjustment factor is introduced in the present work.

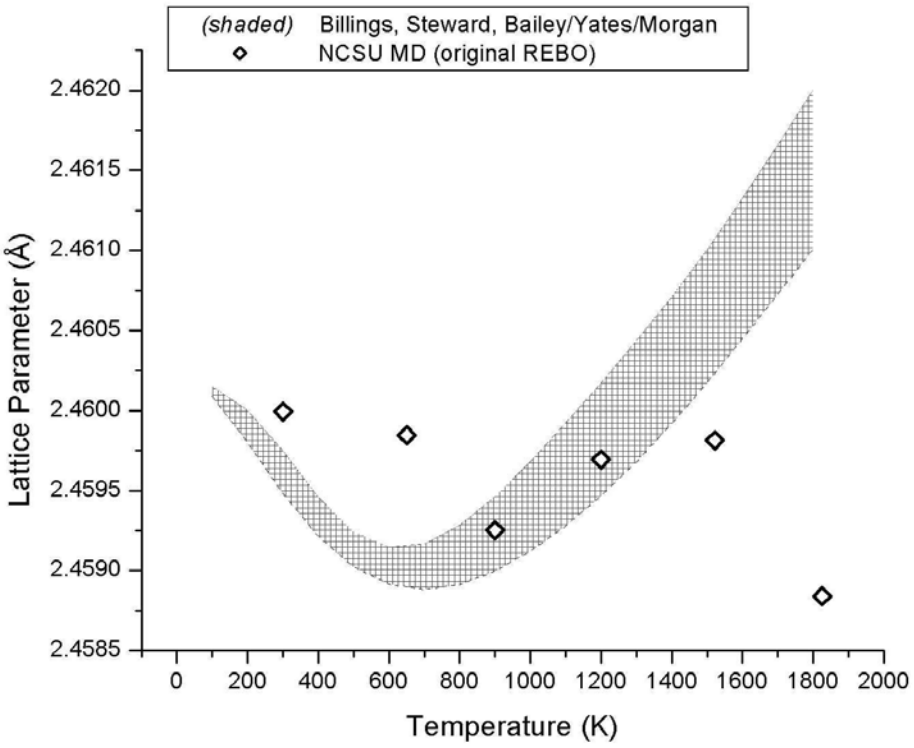

Fig. 3-3 MD calculation of thermal expansion using the published form of the REBO potential (diamonds). MD calculations are compared to a shaded region representing the total range of data reported by Billings [19], Steward [20], and Bailey/Yates/Morgan [21].

Chapter 4

Description of the NCSU MD Model

4.1 Introduction

The final NCSU MD model will now be discussed in detail. A number of non-standard features have been included that specifically address the graphite structure. Unless otherwise noted, all simulations were performed in the NVT ensemble using periodic boundary conditions, at a time step of 0.5 femtoseconds. The flowchart given in Fig. 4-1 illustrates the basic functioning of the NCSU MD code, which is designed to run on parallel processors. Details of the parallelization are discussed in Appendix B.

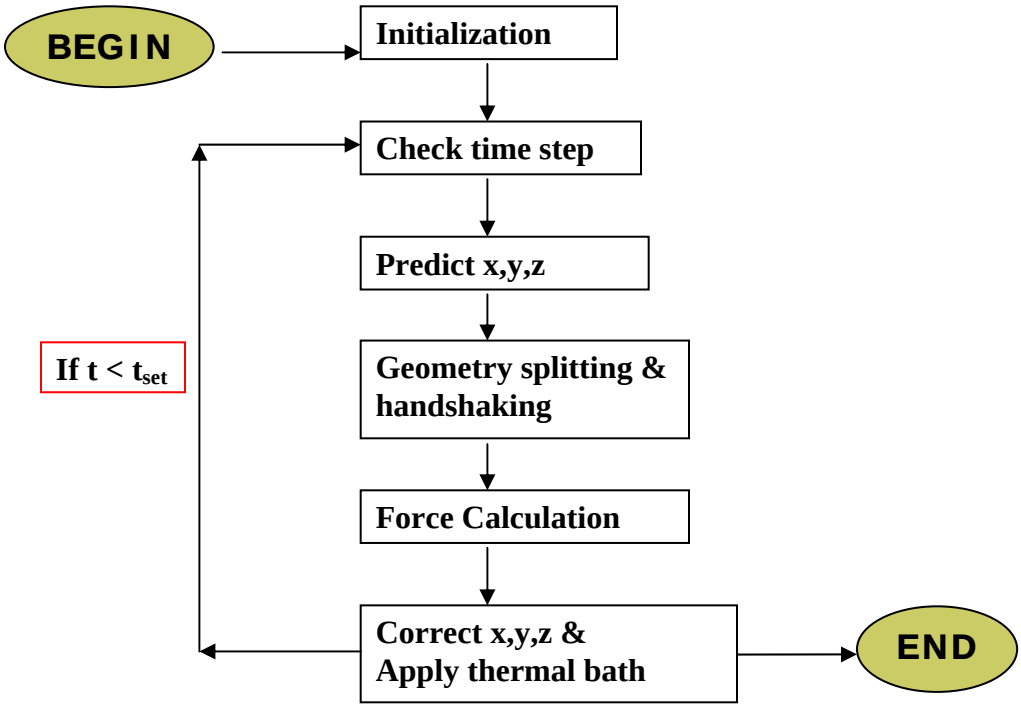

Fig. 4-1 Flowchart of the NCSU MD code

4.2 Thermal Bath

NVT conditions were imposed through a two-step process:

(i) Rescaling of all atomic velocities for several hundred time steps

(ii) Velocity rescaling only within a delimited thermal bath region (along the periphery of the supercell) for the remainder of the simulation

The purpose of step (ii) is to circumvent direct manipulation of atomic trajectories within the interior of the supercell during the "production phase" of the simulation, thereby minimizing perturbation of the system's time evolution. Following equilibration, quantities of interest were calculated as averages over the interior of the supercell (outside of the thermal bath).

4.3 Interplanar spacing

Interplanar separation was automatically computed by the code as a function of temperature and in-plane lattice parameter. The functional form of this relationship was developed by fitting to the (c/a) ratio of graphite at each temperature, as derived from a-axis and c-axis thermal expansion data [14]. Fig. 4-2 shows the (c/a) ratio as a function of temperature. Multiplying the (c/a) ratio by the in-plane lattice parameter (a fixed quantity under the NVT ensemble) results in the correct interplanar spacing.

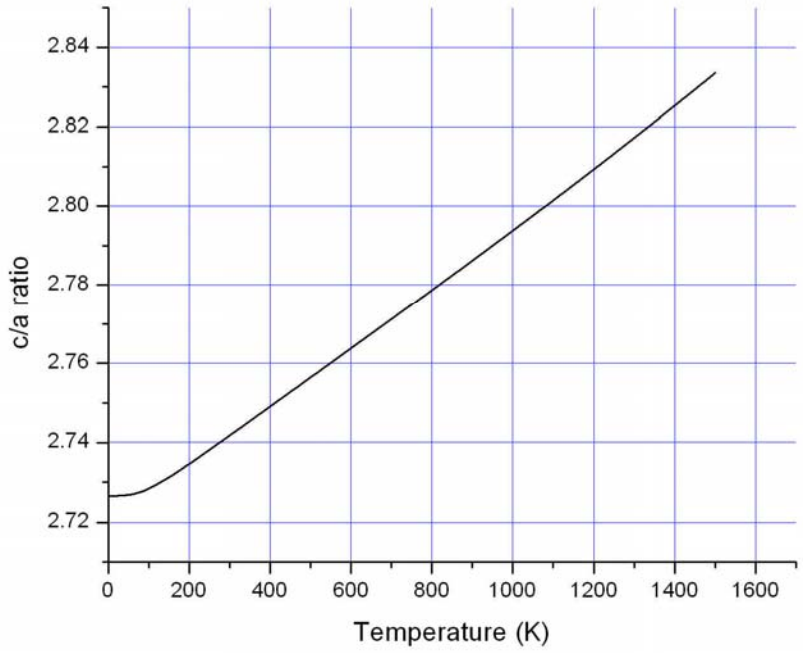

Fig. 4-2 The C/A ratio for Graphite

4.4 Center of Mass Correction

As mentioned in section 2.7, the standard CM correction scheme functions well for an isotropic system yet performs inadequately for graphite. Because the graphitic basal planes do not interact under the REBO potential, it is possible for each plane to glide at some net velocity while still preserving a total CM velocity of zero for the entire system.

This problem was fixed by applying the CM correction on a plane-by-plane basis, thereby precluding the planar glide phenomenon. More precisely, a zero CM velocity condition was enforced in the thermal bath region of the supercell.

4.5 Modifications to the Potential Function

To address deficiencies in the performance of the potential function above 0 K, temperature dependency was introduced into Eq. (2.25), which was re-written as:

$$E = \sum_i \sum_{j>i} f_c'\left(r_{ij,} z, T\right)\left[V_R\left(r_{ij}, T\right) + \overline{b}_{ij} V_A\left(r_{ij}, T\right)\right] \tag{4.1}$$

in which adjustments have been made to the cutoff function and pairwise attractive and repulsive terms. These adjustments are now described in turn.

4.5.1 Anisotropic Cutoff

The cutoff function was augmented with an additional term as follows:

$$f_c'\left(r_{ij,} z, T\right) = f_c\left(r_{ij}\right) + f_c'\left(z, T\right) \tag{4.2}$$

Here, $f_c\left(r_{ij}\right)$ is the standard cutoff function and $f_c'\left(z,T\right)$ is defined as:

$$f_c'\left(z,T\right) = \frac{K\left[1 - \cos\left(\frac{2\pi\ z}{\Delta d}\right)\right]}{2} \tag{4.3}$$

in which z refers to the c-axis displacement of an atom from its initial position in the basal plane, Δd is the interplanar spacing, and K governs the magnitude of the barrier to out-of-plane motion generated by $f_c'\left(z,T\right)$. The appropriate value of K is determined in Chapter 5 by fitting c-axis MSD calculations to experimental measurements.

The basic form of $f_c'\left(z,T\right)$ is plotted in Fig. 4-3. For small displacements, this term exhibits parabolic behavior. Midway between two planes (i.e. at z = Δd/2), the energy contribution from $f_c'\left(z,T\right)$ peaks, as is expected due to symmetry.

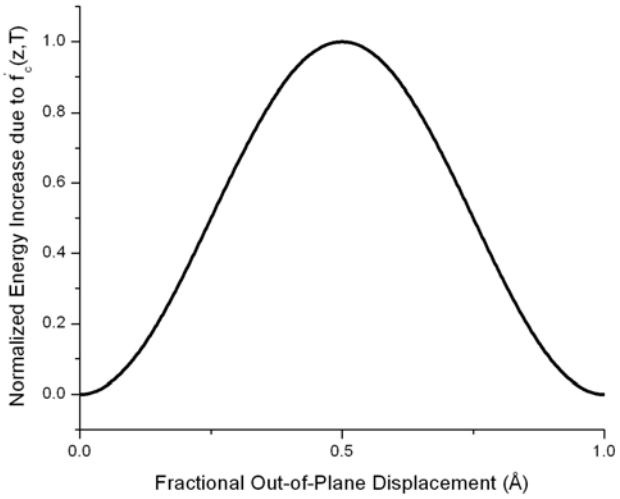

Fig. 4-3 Profile of the c-axis cutoff function, $f_c'(z,T)$. The period of $f_c'(z,T)$ is equal to the interplanar spacing, which increases monotonically with temperature.

The Lennard-Jones model (often used to simulate Van der Waals forces) also behaves parabolically at small displacements about the equilibrium point. This may be demonstrated analytically from the Lennard-Jones formula [16]:

$$U_{lr} = V_e\left[\left(\frac{r_e}{r}\right)^{12} - 2\left(\frac{r_e}{r}\right)^{6}\right] \tag{4.4}$$

where r_e and V_e are fitting constants. Expanding Eq. (4.4) with a Taylor series:

$$\left(\frac{r_e}{r}\right)^{12} \cong 1 - \frac{12}{r_e}(r - r_e) + \frac{78}{(r_e)^2}(r - r_e)^2 + \ldots \tag{4.5}$$

$$-2\left(\frac{r_e}{r}\right)^{6} \cong -2 + \frac{12}{r_e}(r - r_e) - \frac{42}{(r_e)^2}(r - r_e)^2 + \ldots \tag{4.6}$$

And therefore:

$$U_{lr} \cong V_e\left[-1 + \frac{36}{(r_e)^2}(r - r_e)^2\right] \tag{4.7}$$

at small displacements from r_e (the minimum energy distance).

4.5.2 Pairwise Coefficients

The terms $V_A(r_{ij},T)$ and $V_R(r_{ij},T)$ in Eq. (4.1) may be expanded as:

$$V_R(r_{ij},T) = A(T)\left[1+\frac{Q}{r_{ij}}\right]\exp\left[-\alpha r_{ij}\right] \tag{4.8}$$

$$V_A(r_{ij},T) = \sum_{n=1,3} B_n(T)\exp\left[-\beta_n r_{ij}\right] \tag{4.9}$$

where the pairwise potential coefficients, A and B_n, now vary with temperature. The purpose of this modification is to compensate for the sole usage of 0 K properties in fitting the interatomic potential function, which was shown to be inadequate for graphite even at intermediate temperatures.

Modification of the pairwise coefficients affects the weights of the repulsive and attractive terms, and any change in these coefficients will, in general, affect both the position and depth of the potential energy minimum. Because the thermal expansion coefficient depends upon the position of the potential energy minimum as a function of temperature, correct thermal expansion behavior may be achieved by devising appropriate forms for $A(T)$ and $B_n(T)$. The specific methodology used in this work to define $A(T)$ and $B_n(T)$ will be discussed in Chapter 5.

Chapter 5

MD Results

5.1 Absolute Zero Properties

The first step in verifying an interatomic potential function is to ensure that it yields correct values for the physical parameters of the system of interest at absolute zero temperature. Two such parameters – the cohesive energy and bond length – are characteristic quantities that are generally well-defined in literature. Fortunately, both are also obtainable from the most basic output of an MD simulation.

The cohesive energy of a crystal is defined as the energy required to dissociate the crystal into a set of infinitely separated atoms at rest [16]. Because the REBO potential does not account for interplanar interaction, determination of the cohesive energy in graphite involves only the in-plane lattice parameters (the *a* and *b* parameters). These are related by:

$$b = \frac{2}{\sqrt{3}} a \tag{5.1}$$

so that the cohesive energy is a function only of the *a* parameter.

To calculate cohesive energy using the NCSU MD code, the system temperature was held at 0 K and potential energy was calculated at various in-plane lattice parameters ranging between 2.44 Å and 2.48 Å. The supercell size was set to 1024 atoms and the total simulation time was fixed at 1.5 picoseconds with a 1.0 femtosecond time step. The resulting curve of crystal energy vs. lattice parameter is given in Fig. 5-1.

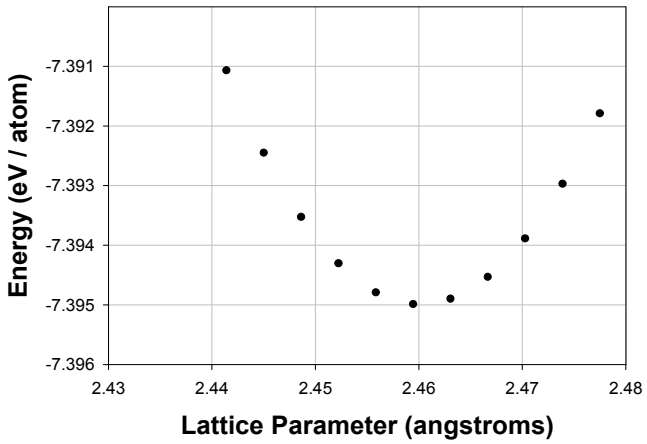

Fig. 5-1 The energy profile as a function of lattice parameter at 0K

Theoretically, the 0 K properties of graphite correspond to the minimum of the energy curve. The deduced equilibrium lattice parameter is therefore 2.46 Å, and the cohesive energy (i.e. the potential energy at the equilibrium lattice parameter) is 7.395 eV/atom. These values exhibit good agreement with experiment as well as previously published results with the REBO potential function [12].

5.2 General High Temperature Behavior

5.2.1 Potential Energy

Prior to parameterizing the REBO potential to fit temperature-dependent physical properties, a few relatively simple calculations were performed to verify that the code was functioning properly at high temperatures. First, the average potential energy of the system was examined as a function of temperature between 0K and 1800K. For a perfectly harmonic system, the magnitude of the potential energy is expected to decrease linearly with temperature as per the relation:

$$E = E_{tot} - E_K \cong E_{coh} - \frac{3}{2}kT \tag{5.2}$$

where E_{coh} is the cohesive energy. While the simulated system is not expected to behave in a purely harmonic manner, Eq. (5.2) should be a rough approximation of the calculated mean potential energy. MD calculations of potential energy are compared to the harmonic approximation in Fig. 5-2.

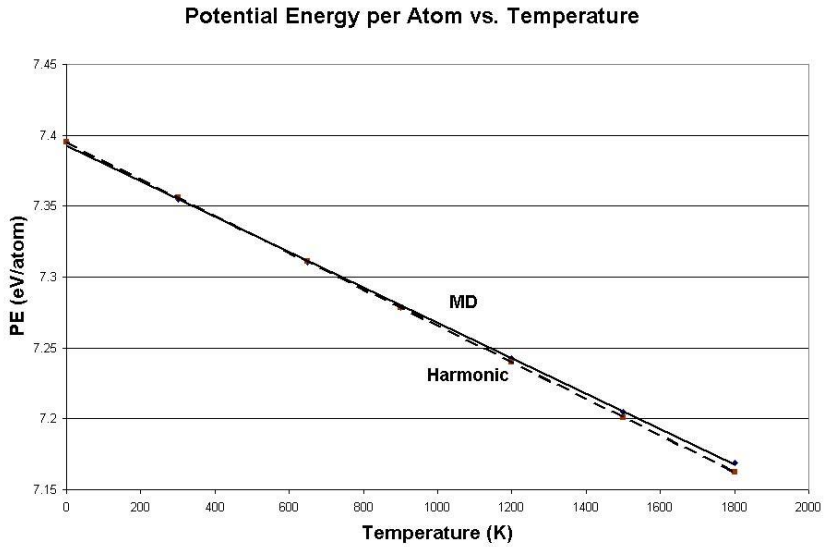

Fig. 5-2 Mean potential energy vs. temperature. Comparison is made to the harmonic approximation.

Anharmonicity in the potential function is evident through the slight deviation from the harmonic approximation. However, the average MD potential energy exhibits very similar behavior.

5.2.2 Standard Deviation in Temperature

Another simple test involves the standard deviation in temperature. For the purposes of this test, the simulated graphite system was equilibrated under the NVT ensemble and the

temperature control mechanism was then halted abruptly, converting the system to an NVE (constant energy) ensemble. Under the NVE ensemble, the average kinetic energy (and hence also the temperature) fluctuates with an amplitude dependent upon the magnitude of the temperature. To see this, one may start with the statistical uncertainty inherent in one particle's kinetic energy:

$$\sigma_{E_K} = k_B T \tag{5.3}$$

where the total kinetic energy of the system is given by $\varepsilon = NE_K$. Therefore,

$$\sigma_\varepsilon = \sqrt{\sum_i \left(\Delta E_{Ki}\right)^2} = \sqrt{N\left(k_B T\right)^2} = k_B T\sqrt{N} \tag{5.4}$$

and from the classical expression relating kinetic energy to temperature:

$$\varepsilon = \frac{3}{2} N k_B T \tag{5.5}$$

the standard deviation in temperature can be derived as follows:

$$\sigma_\varepsilon = \frac{3}{2} N k_B \sigma_T = k_B T\sqrt{N} \tag{5.6}$$

$$\sigma_T = \frac{2}{3} T \frac{1}{\sqrt{N}} \tag{5.7}$$

To compare this theoretical relation against MD, the standard deviation in temperature was directly calculated after applying a 1500 K thermal bath for 1.0 picoseconds followed by 2.0 picoseconds of unconstrained (NVE) equilibration. Fig. 5-3 shows a comparison between σ_T computed during the NVE phase and the standard deviation predicted from Boltzmann statistics [17], as derived above. The close correspondence apparent in Fig. 5-3 suggests appropriate MD behavior at high temperatures [18].

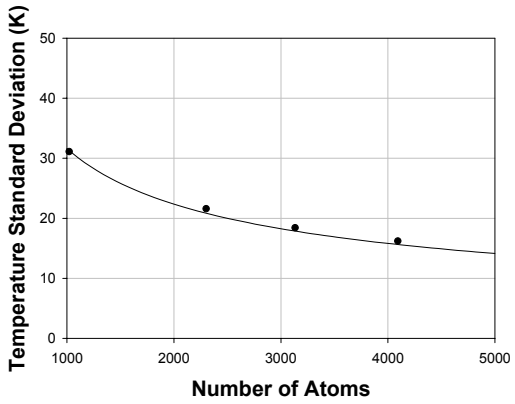

Fig. 5-3 Comparison of the temperature fluctuations of a graphitic system as calculated from MD simulations (dots) and the derived theoretical model (solid curve).

5.3 High Temperature Physical Properties

5.3.1 Thermal Expansion

The linear coefficient of thermal expansion is defined as:

$$\alpha(T) = \frac{1}{a(T)} \frac{da(T)}{dT} \tag{5.8}$$

where $a(T)$ is the lattice parameter at temperature T. In a purely harmonic material, the coefficient of thermal expansion is uniformly zero. Thus, expansion (or contraction) arises from higher-order anharmonic terms in the potential energy function.

In non-cubic materials, α(T) generally exhibits distinct behavior along each crystallographic axis. This fact is particularly evident in graphite, which expands monotonically along the c-axis while showing a contraction effect along the a-axis at low temperatures, transitioning to a slow expansion above about 650 K. The difference in the expansion profile between these two axes arises from the vast dissimilarity in bonding character.

As a consequence of the short-range nature of the REBO potential, the c-axis expansion coefficient could not be examined in this work. However, the a-axis expansion coefficient is an excellent quantity against which to benchmark the NCSU MD code.

Adjustment Factor

It has already been shown that thermal expansion calculations using the published REBO potential do not agree well with experiment. Thus, the discussion now focuses on fitting the functions $A(T)$ and $B_n(T)$ (as applied in Eqs. (4.8) and (4.9)) to the correct thermal expansion profile of graphite. For the purposes of this work, $A(T)$ and $B_n(T)$ were written as:

$$A(T) = A_o \exp[\alpha C(T) T] \tag{5.9}$$

$$B_n(T) = B_{n,o} \exp[\beta_n C(T) T] \tag{5.10}$$

where A_o and $B_{n,o}$ are the constant pairwise coefficients as defined in the published REBO potential, and C(T) is a temperature-dependent adjustment factor. These forms for $A(T)$ and $B_n(T)$ were chosen because they reduce to A_o and $B_{n,o}$ at T = 0, thereby maintaining agreement with 0 K properties such as bond length and cohesive energy. The procedure employed to obtain an explicit formula for C(T) shall now be described.

First, an estimation of the sensitivity of the potential energy minimum to C(T) is needed. Due to the small magnitude of the adjustment factor – which is treated as a perturbation to the potential function – the terms $\exp[\alpha C(T) T]$ and $\exp[\beta_n C(T) T]$ are approximately linear within the temperature range of interest, and consequently the position

of the potential energy minimum is also linear with respect to C(T)T. Therefore, an estimation of C(T) at any temperature may be ascertained via the formula:

$$C_{est}(T) = \frac{C}{\Delta a}\left[a_{ref}(T) - a_o(T)\right] \tag{5.11}$$

where C_{est} is the estimated adjustment factor, a_{ref} and a_o are the reference and calculated lattice parameters respectively, and Δa/C is the rate of change in lattice parameter with respect to C (generated from an arbitrary yet reasonable initial guess of C).

It is sufficient to determine the slope, Δa/C, at one temperature (say 300K) and then utilize this to estimate the value of C(T) required to match experimental data at all other temperatures. Using the procedure outlined above, the normalized slope, $\frac{\Delta a}{C(T)T}$, was found to be 0.87.

Applying Eq. (5.11) to the data in Fig. 3-3 results in the estimated C(T) values plotted in Fig. 5-4. The reference lattice parameters were taken as the midpoints of the shaded region of Fig. 3-3.

While the data in Fig. 5-4 appear to be roughly linear, a simple linear (or polynomial) fit would be inappropriate for graphite. This is because graphite expands at a nearly constant rate in both the low and high temperature extremes, whereas a polynomial fit would result in an accelerating expansion throughout the entire range of temperatures.

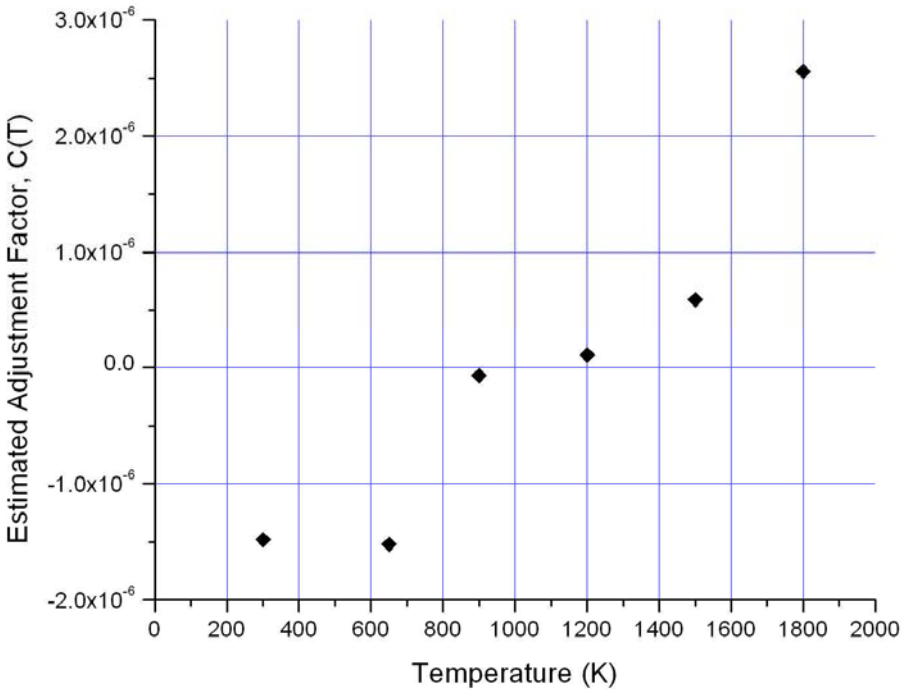

Fig. 5-4 The predicted values of C(T) up to 1800 K.

A sigmoidal fit was chosen because the sigmoid function asymptotically approaches constant values at the low and high temperature extremes, resulting in a constant thermal expansion (or contraction) in these limits, as is observed in graphite. To fit the data of Fig. 5-4, a four-parameter sigmoid function of the following form was used:

$$C(T) = c_o + \frac{b}{1 + \exp\left[\frac{-(T - T_o)}{d}\right]} \tag{5.12}$$

in which c_o, b, d, and T_o are fitting parameters. SIGMAPLOT was employed to compute these parameters through nonlinear least-squares regression analysis. The fitted values are tabulated in Table 5.1. Applying the parameterization of Table 5.1 to Eq. (5.12) generates the C(T) function plotted in Fig. 5-5.

Table 5.1: Parameters for Sigmoidal Fit to C(T).

b	=	4.769E-06 Å/K
d	=	3.897E+02 K
T_o	=	1.410E+03 K
c_o	=	-1.681E-06 Å/K

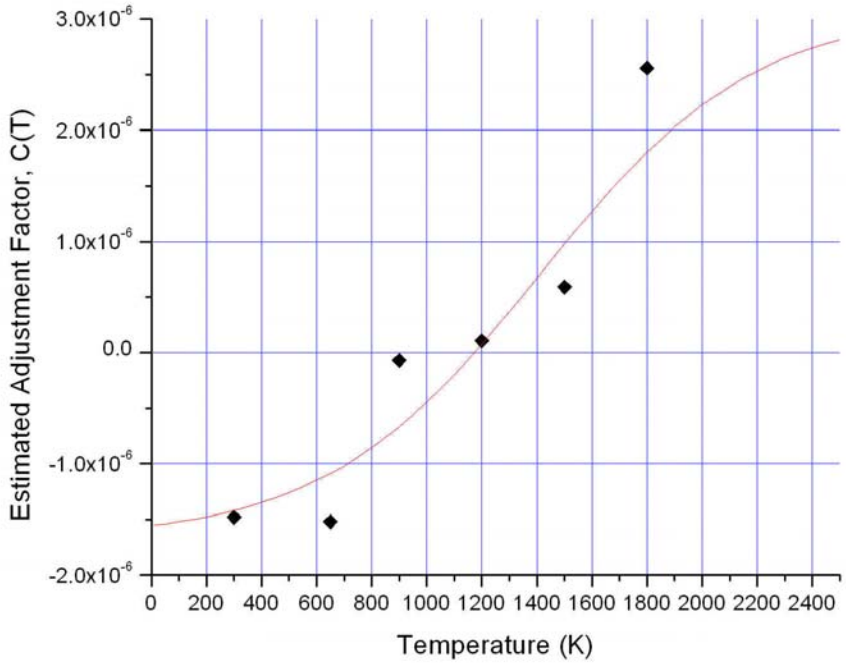

Fig. 5-5 Sigmoidal Fit to the estimated values of C(T)

Substituting the fitted C(T) back into Eqs. (5.9) and (5.10) yields the final formulae for $A(T)$ and $B_n(T)$, which are plotted in Fig. 5-6 Lattice parameter computations were repeated to confirm that $A(T)$ and $B_n(T)$ generate the desired impact on thermal expansion behavior. The resulting thermal expansion profile, displayed in Fig. 5-7, almost completely coincides with the shaded band of reference data.

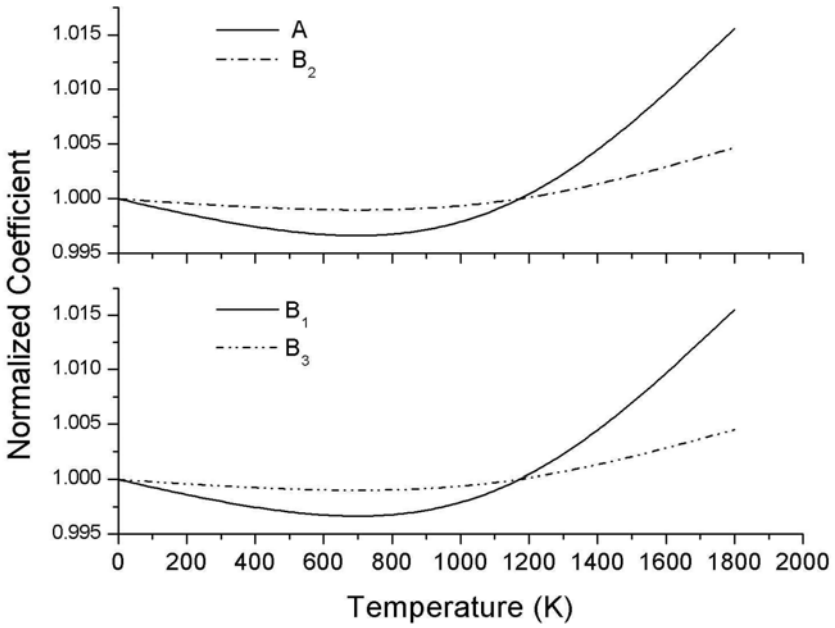

Fig. 5-6. Attractive and repulsive coefficients of the modified REBO potential as a function of temperature, normalized to their (constant) published values. At 0 K the normalized coefficients are identically unity, indicating that there is no impact to the cohesive energy or bond length at this temperature.

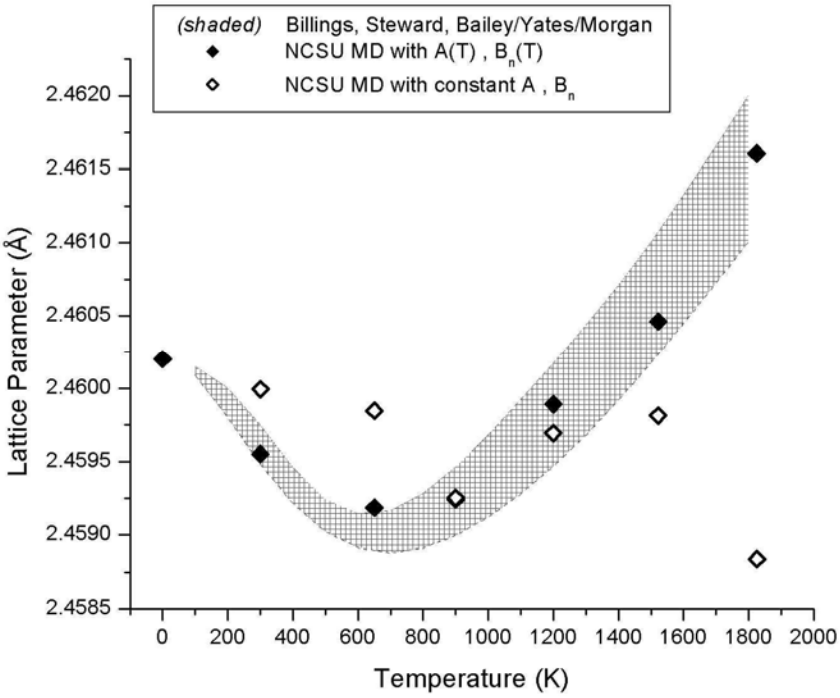

Fig. 5-7. The effect of C(T) on thermal expansion. MD calculations are compared to a shaded region representing the total range of data reported by Billings [19], Steward [20], and Bailey/Yates/Morgan [21].

The MD calculations plotted in Fig. 5-7 represent the minimum energy lattice parameters as determined through polynomial regression analysis. These fits are shown in Fig. 5-8. At each lattice parameter and temperature, the system was evolved until convergence was observed in the potential energy as a function of time. Average values of the potential energy were computed over the last several thousand steps of the run.

To illustrate the convergence of the results presented in Fig. 5-8, the standard error of the mean potential energy at 1822 K (the most restrictive case) is shown in Fig. 5-9 for each lattice parameter used in the polynomial fitting. In all cases, the standard error was found to be on the order of 10^{-5} eV – much less than the typical difference between successive energy calculations. The energies used in the polynomial fitting routine are therefore relatively well defined, and a fit may be applied with confidence.

One consequence of adding temperature dependence to the pairwise potential coefficients is that the minimum of the interatomic potential energy curve is slightly shifted at each temperature. This effect is demonstrated in Fig. 5-10 at temperatures of 300, 900, and 1800 K. As expected, the position of the minimum potential energy as a function of temperature follows the same trend as the lattice parameter. The changes in potential energy due to C(T) are only on the order of 0.1%, indicating that C(T) is indeed acting as a small perturbation.

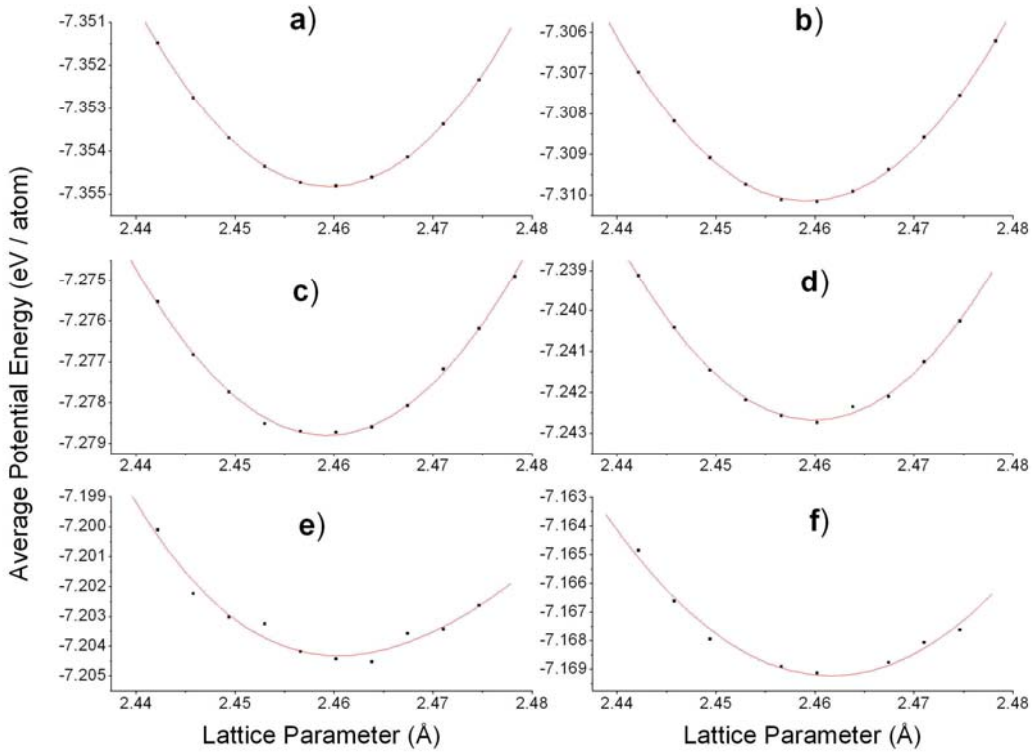

Fig. 5-8: The average potential energy as a function of lattice parameter at: a) 300 K , b) 650 K , c) 900 K , d) 1200 K , e) 1520 K , and f) 1822 K using the temperature-adjusted REBO potential. The minima of the polynomial fits correspond to the lattice parameters at thermal equilibrium.

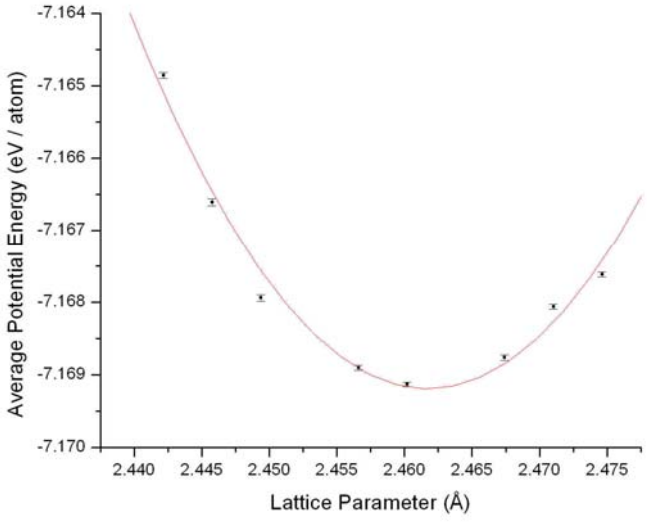

Fig. 5-9. Computations of the average potential energy at 1822 K, with error bars representing the standard error in the sample mean. This error is on the order of 10^{-5} eV.

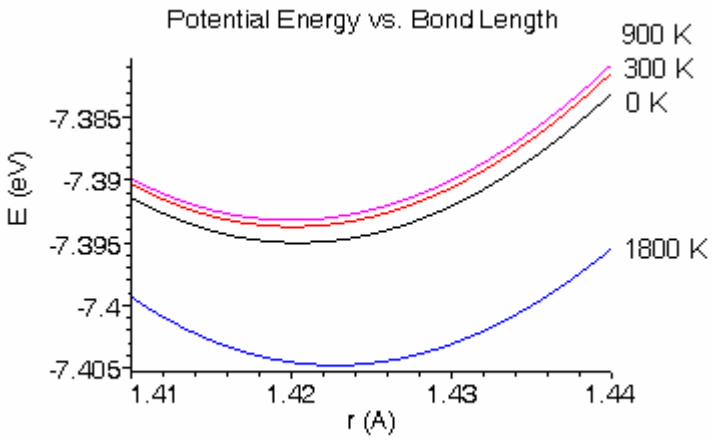

Fig. 5-10 The impact of C(T) on the interatomic potential energy curve

5.3.2 Mean Squared Displacement

The mean-squared displacement (MSD), calculated in MD from the equation:

$$MSD = \left\langle \Delta^2 r \right\rangle = \frac{\sum_{t=T_o}^{T} \sum_{n=1}^{N} \left[r_n^t - r_n^0 \right]^2}{(N)(T - T_o)} \tag{5.13}$$

is a measure of the average distance by which a particle deviates from its initial position. Here, r_n^t refers to the instantaneous displacement from equilibrium of particle *n* at time *t*, *N* is the total number of particles, T_o is the initial time step, T is the final time step, and $(T\text{-}T_o)$ is the total number of time steps over which MSD is calculated.

Solids, liquids, and gases exhibit fundamental differences in the time evolution of MSD. Representative MSD curves of the three states of matter are displayed in Fig. 5-11. In a gas, the weakness of the interatomic interaction allows atoms to expand almost freely, giving rise to a parabolically increasing MSD. Liquid particles are in close contact and

significantly impede each other's movement. Consequently, the atoms in a liquid move almost in the fashion of a random walk, resulting in a linearly increasing MSD following an initial transient period. Particles in a solid, on the other hand, are confined to discrete lattice positions under normal conditions. The MSD therefore fluctuates about a definite mean value that depends upon the temperature and interatomic binding characteristics of the system.

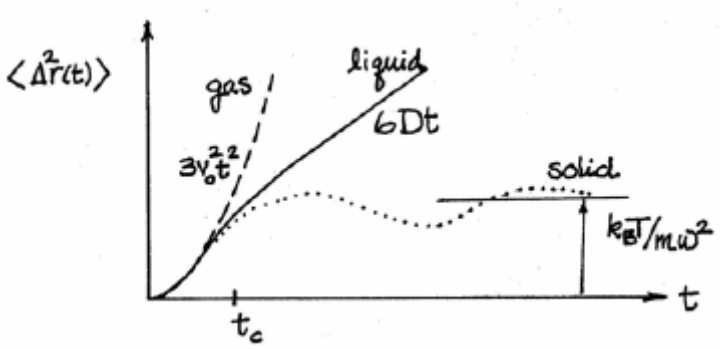

Fig. 5-11: Representative MSD profiles of a solid, liquid, and gas. [22]

In addition to the total MSD (represented by Eq. (5.13)), one could also compute the partial MSD along any arbitrary axis by replacing the *r* of Eq. (5.13) with the displacement along the chosen axis. In the Cartesian coordinate system, the partial and total MSD are related by:

$$\left(\Delta^2 r\right)^2 = \left(\Delta^2 x\right)^2 + \left(\Delta^2 y\right)^2 + \left(\Delta^2 z\right)^2 \tag{5.14}$$

where, in the case of a cubic system, one would expect the three terms on the RHS to be equal due to symmetry. However, in an anisotropic system, the partial MSDs generally take on distinct values based on the binding characteristics along each axis. This is particularly true for graphite, in which large out-of-plane displacements result from the weakness of the

Van der Waals force acting between basal planes. In fact, the amplitude of c-axis thermal vibrations is roughly an order of magnitude greater than that of in-plane vibrations.

Examples of the time evolution of MSD as computed with the NCSU MD code are given in Fig. 5-12. The system begins in an unperturbed state, corresponding to an MSD of zero along each axis. As the carbon atoms move outward with an average kinetic energy proportional to the system temperature, MSD increases rapidly and generally assumes a maximum before leveling off about an equilibrium value. Once steady-state fluctuation is apparent, a reliable average value can be extracted over several thousand time steps.

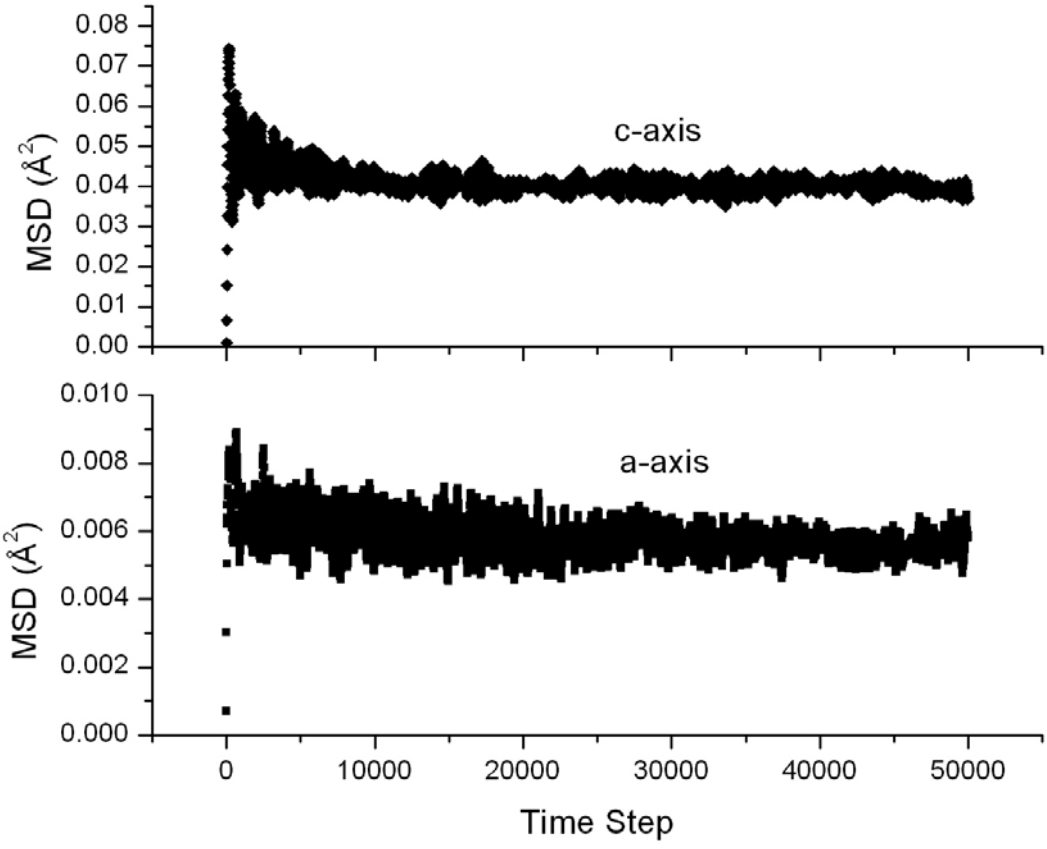

Fig. 5-12 The asymptotic convergence of the graphitic a-axis and c-axis MSD at 1200 K.

The out-of-plane MSD was fitted through the function $f_c^{'}(z,T)$, defined in Eq. (4.3). Specifically, the coefficient *K* was determined so as to optimize the match between the c-axis MSD and the range of relevant theoretical and experimental data (given in Fig. 5-13). Because the pairwise attractive and repulsive terms are modulated by $f_c^{'}(z,T)$, the product has units of energy and one expects that:

$$f_c^{'}(z,T)\left[V_R(r_{ij})+\bar{b}_{ij}V_A(r_{ij})\right] \sim E_{\Delta d} \tag{5.15}$$

where $E_{\Delta d}$ is the interlayer binding energy of graphite (measured to be in the range of of 50-60 meV/atom [28]). Optimizing *K* using Eq. (5.15) to generate an initial guess, the value of *K* was found to be 0.00533, which produces good agreement with literature MSD data throughout the temperature range of interest. Substitution of the cohesive energy of graphite into the bracketed term of Eq. (5.15) yields $E_{\Delta d} \cong$ 40 meV at the optimized value of *K*.

With the fitted function $f_c^{'}(z,T)$ incorporated into REBO, the NCSU MD code was used to compute MSD (both in-plane and out-of-plane) at temperatures ranging from 0 K to 1800 K. In terms of Cartesian coordinates, the in-plane and out-of-plane MSD are defined respectively as:

$$\left\langle \Delta^2 r \right\rangle_{in} = \sqrt{\left\langle \Delta^2 x \right\rangle^2 + \left\langle \Delta^2 y \right\rangle^2} \tag{5.16}$$

$$\left\langle \Delta^2 r \right\rangle_{out} = \left\langle \Delta^2 z \right\rangle \tag{5.17}$$

where *z* is oriented along the hexagonal c-axis. Each simulation was run for 50,000 time steps, with the MSD averages taken over the final 30,000 steps. In each case, convergence was verified by constructing plots similar to Fig. 5-12. The results are shown in Fig. 5-13.

It should be noted that the computed MSD is uniformly zero at 0 K, whereas the reference curves included in Fig. 5-13 tend toward nonzero values at 0 K. This inconsistency

arises from the classical nature of MD. In a real system, atomic vibrations (termed "zero point vibrations") occur even at 0 K as a consequence of Heisenberg's uncertainty principle. An MD system at 0 K, however, possesses no internal energy and therefore contains only static atoms. The inability of MD to account for zero point vibration is one example of the breakdown of MD techniques in the low temperature limit.

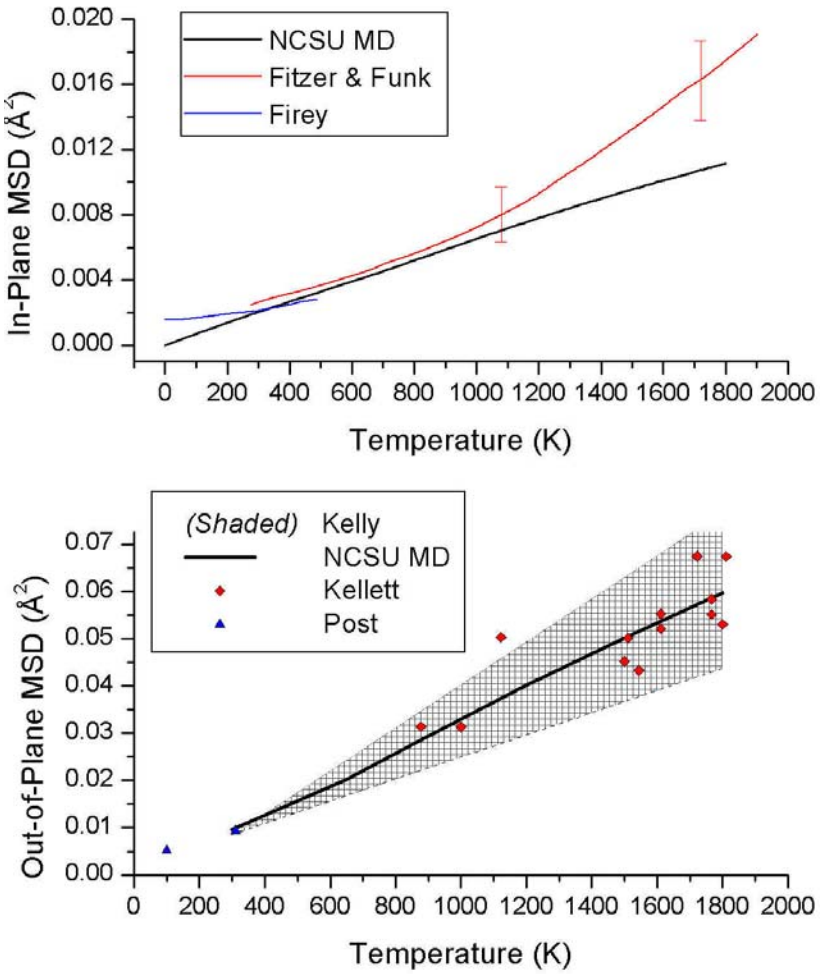

Fig. 5-13: TOP PANEL: The in-plane MSD as compared with the x-ray diffraction measurements of Fitzer & Funk [23] and the lattice dynamical calculation of Firey [24]. BOTTOM PANEL: The out-of-plane MSD as compared with the theoretical upper and lower bounds proposed by Kelly [25]. Experimental measurements are represented by red diamonds (Kellet [26]) and blue triangles (Post [27]).

While the out-of-plane MSD exhibits very good agreement with experiment, the computed in-plane MSD begins to diverge from the measurements of Fitzer & Funk at about 1100 K – the point at which the Fitzer & Funk data suddenly curves upwards. This change in slope is believed to result from the large magnitude of the in-plane Debye temperature (1500 K), which causes additional modes of vibration to be activated at high temperatures [23]. Because the out-of-plane Debye temperature is much lower (625 K), no sudden change of slope is evident in the c-axis MSD at intermediate to high temperatures.

5.3.3 Bond Length

In addition to the insight gained from MSD concerning the vibrational characteristics of graphite atoms, the behavior of the interatomic bond length (corresponding to the relative displacement of neighboring atoms) also provides information about the dynamics of the system. A representative plot of the time evolution of bond length is given in Fig. 5-14.

As is apparent in Fig. 5-14, the minimum, maximum, and average bond length all approach steady mean values after roughly 10,000 steps. Because of the steep repulsive barrier inherent to the REBO potential, the minimum bond length is closer to the mean value than is the maximum bond length. Notably, a small number of atoms enter the cutoff range of the potential function (1.7 Å – 2.0 Å), but this occurs far too infrequently to impact the equilibrium properties of the system within the temperature range of interest.

Whereas the minimum and maximum bond length fluctuate considerably, the average bond length assumes a very well defined value that varies with temperature as shown in Fig. 5-15.

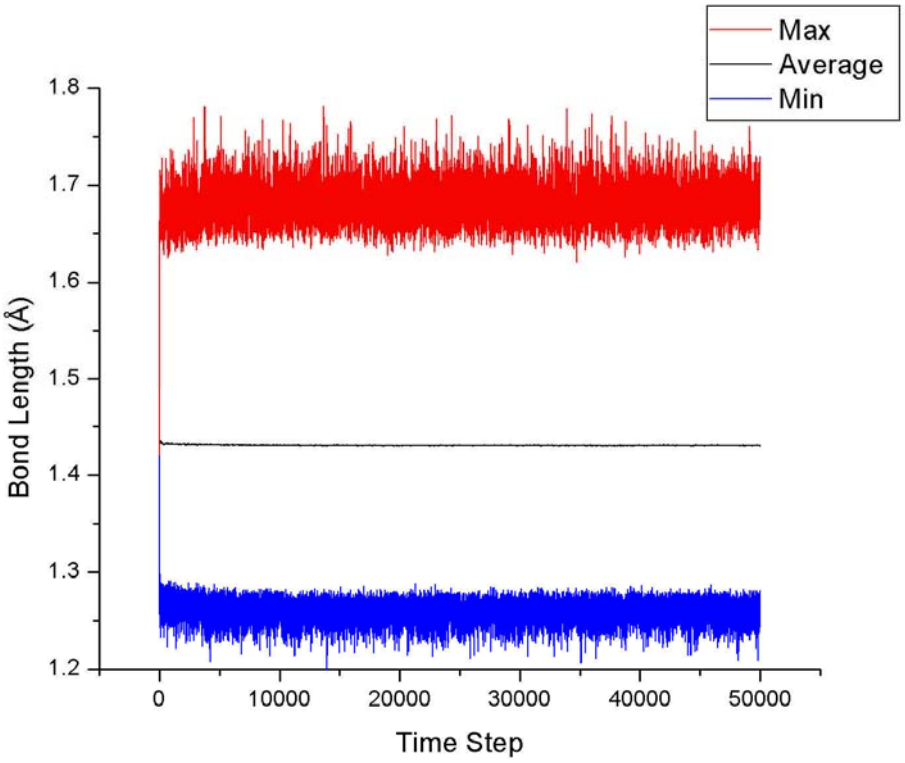

Fig. 5-14. The evolution of the minimum, maximum, and average interatomic bond length during the course of a 1500 K NCSU MD simulation.

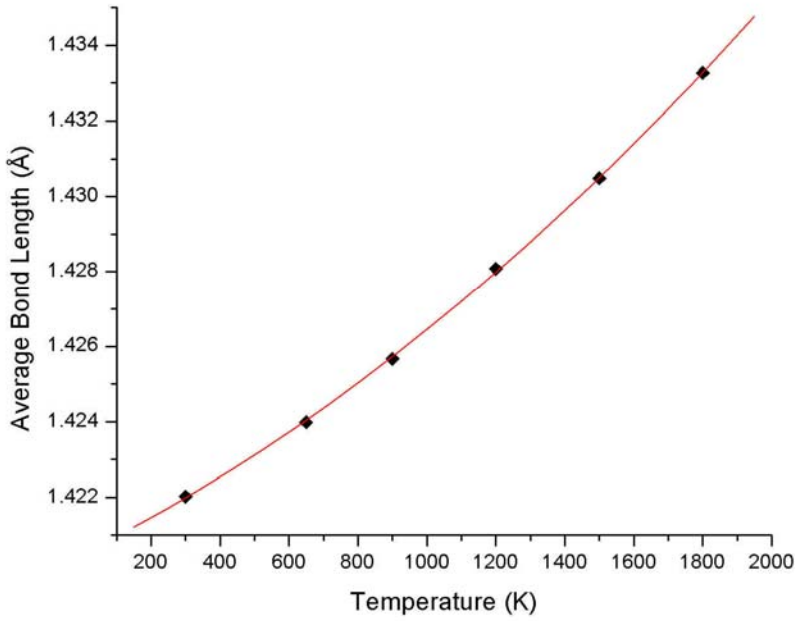

Fig. 5-15. The increase in average interatomic distance (bond length) with temperature. A 2nd order polynomial fit is superimposed on the data.

The monotonic increase in mean bond length arises due to anharmonicity in the potential energy function. Even though the basal plane contracts at low to intermediate temperatures, the mean interatomic distance nevertheless exhibits continual expansion. This seeming contradiction is made possible by the relative freedom of out-of-plane atomic motion, which factors explicitly into bond length but does not directly affect basal plane expansion.

5.3.4 Radiation Damage & Threshold Displacement Energy

When an impinging high energy particle interacts with the constituent atoms of a material, it is possible for one (or more) atoms to gain sufficient energy to produce a defect in the regular lattice structure. Typically, irradiation generates vacancy - interstitial pairs termed Frenkel defects, which can interact to form more complex defect networks. If the environment of the defect contains adequate thermal energy, diffusion of the defect back to its original lattice site (i.e. recombination) may take place. Otherwise, the defect becomes a permanent part of the material structure.

In a nuclear reactor, the moderator material (e.g. graphite) will normally be bombarded with neutrons in the MeV range of energy. Each collision between an incident neutron and a moderator atom creates a highly energetic projectile – denoted the primary knock-on atom (PKA) – which recoils with an energy proportional to the energy of the incident neutron. Generally, the PKA energy lies within the keV range. The energy of the PKA is, in turn, dissipated in collisions with other moderator atoms, possibly creating a number of defects before an equilibrium state is reached. The colliding neutron may also undergo subsequent collisions and create multiple PKAs prior to thermalization.

An important quantity in predicting the degree of damage to the moderator structure is the threshold displacement energy (E_d), defined as the minimum PKA energy sufficient to create a stable Frenkel pair. E_d is significant because its inverse serves as a rough constant of proportionality between the amount of energy deposited in the moderator and the resulting number of defects produced (prior to recombination). Since the quantity of defects exerts a sizable influence on physical and mechanical properties (particularly conductivity), E_d plays a vital role in radiation damage studies.

The threshold displacement energy is readily calculable using MD techniques; this procedure is outlined in Fig. 5-16. Essentially, PKAs of increasingly large energy are introduced sequentially into an otherwise unperturbed supercell until a Frenkel pair remains after the reinstatement of thermal equilibrium. The lowest energy at which this occurs is recorded as E_d.

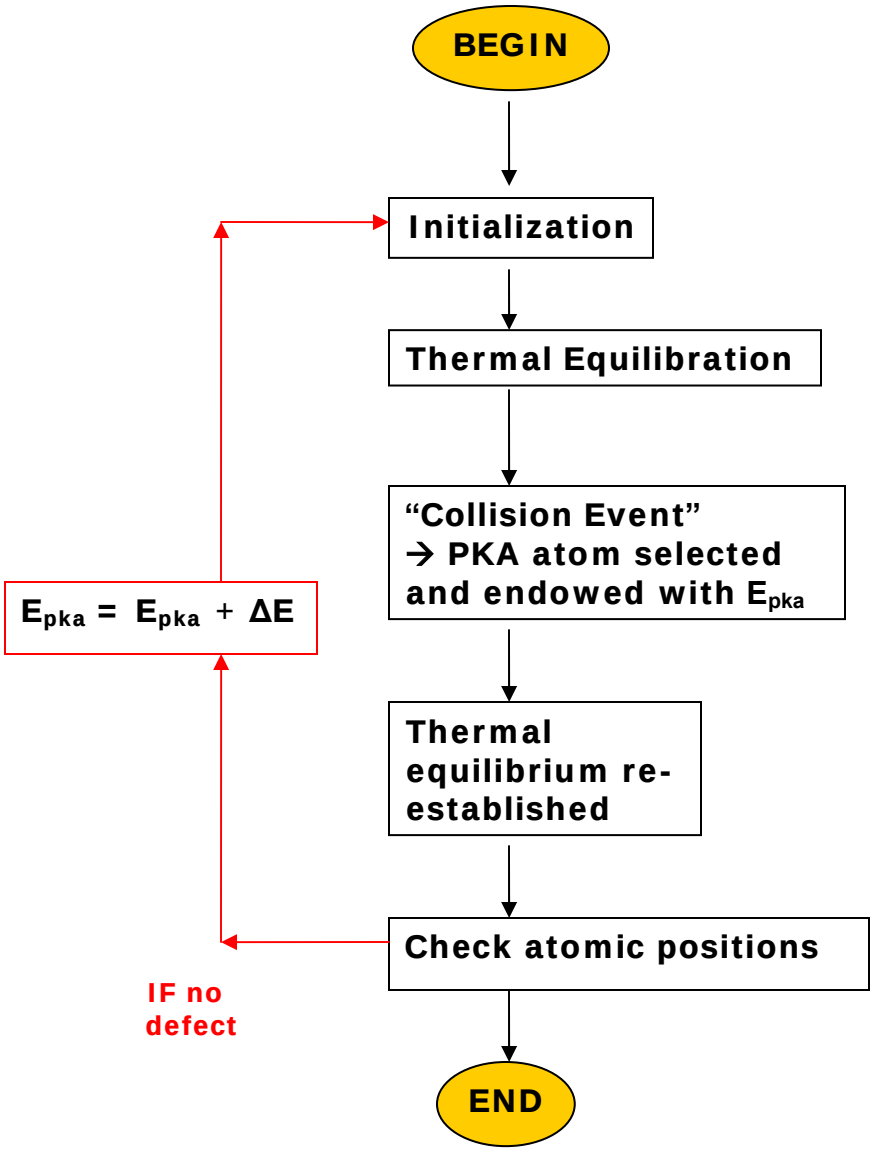

Fig. 5-16. Schematic of the MD routine for determining the threshold displacement energy (E_d).

Because of graphite's anisotropic structure, there exists a range of non-equivalent PKA directions bounded by polar and azimuthal angles of:

$$\theta = [0° - 60°]$$

$$\Phi = [0° - 90°]$$

where θ is the polar (in-plane) angle and Φ is the azimuthal angle from the c-axis. Furthermore, two distinct lattice sites exist – those with honeycomb gaps directly above and below (AB type), and those with carbon atoms above and below (AA type). A schematic of the format used in defining features of the PKA is given in Fig. 5-17. To comprehensively investigate E_d, sufficient permutations of the polar and azimuthal angles (using both AA and AB type PKAs) must be examined.

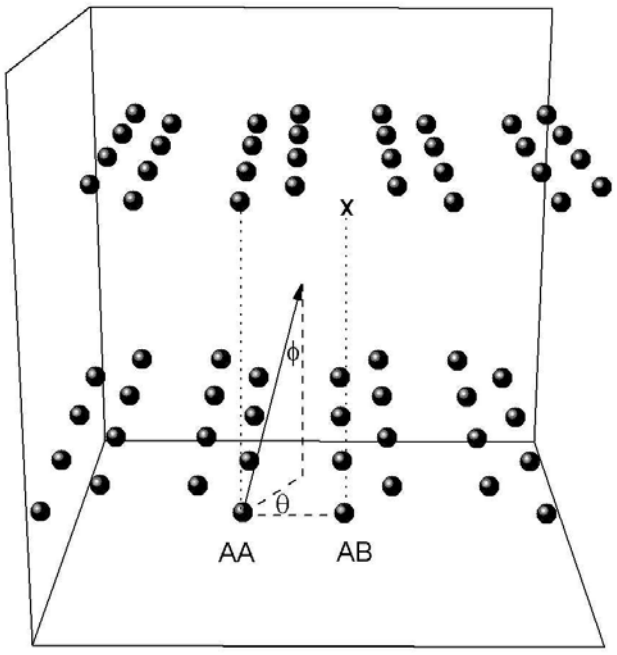

Fig. 5-17. The notation used in defining the PKA type and orientation. Θ refers to the polar angle while Φ denotes the azimuthal angle from the c-axis. AA type atoms are situation directly above and below other carbon atoms, whereas AB types lie between two honeycomb gaps (represented by the "x" symbol). Θ and Φ span non-equivalent ranges of [0° - 60°] and [0° - 90°] respectively.

The investigated angular permutations are elaborated in Table 5.2, from which it is apparent that a total of 28 E_d calculations were performed at each temperature (14 permutations x 2 non-equivalent atoms). The results of these calculations are presented in Fig. 5-18.

Table 5.2: The PKA directions along which E_d was computed

Φ(°)	θ(°)	Note
0	0	purely out-of-plane
30	0,20,40,60	
60	0,20,40,60	
90	0,15,30,45,60	purely in-plane

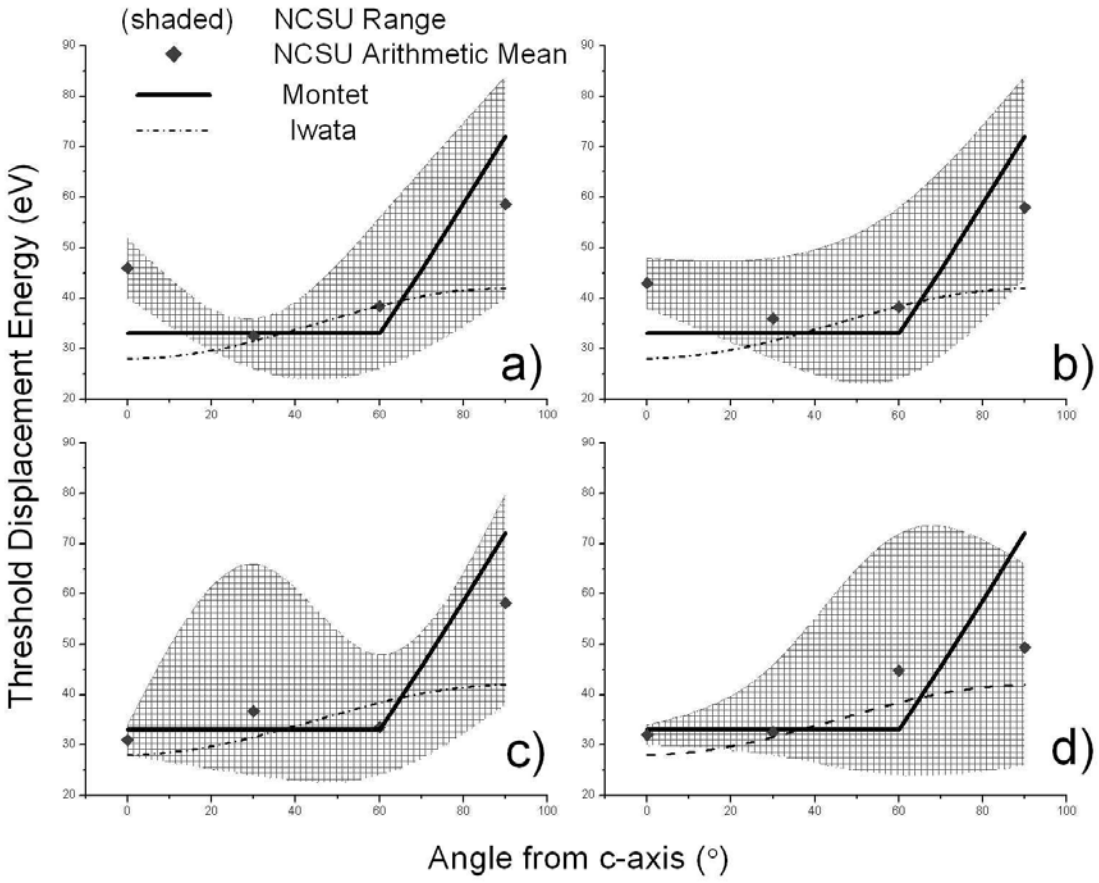

Fig. 5-18. The threshold displacement energy of graphite at: a) 300 K, b) 700 K, c) 1200 K, and d) 1800 K. The shaded area represents the total calculated range of E_d with respect to polar angle and atom type. Θ-averaged E_d is plotted as solid diamonds. MD results are compared to the electron irradiation studies of Montet [29] and Iwata [30], both conducted at approximately room temperature (298 K).

As expected, the θ-averaged threshold displacement energy attains a maximum value at $\Phi = 90°$ – the angle corresponding to a purely in-plane PKA. This result arises from the fact that in-plane PKAs collide with other carbon atoms in the same honeycomb cluster as the PKA, thereby causing the PKA to slow down in the vicinity of its associated vacancy. In this situation, recombination is likely to occur.

PKAs with an out-of-plane component (i.e. with $0° \leq \Phi < 90°$) do not necessarily collide with a carbon atom of the same plane. Especially below $\Phi = 60°$, the PKA tends to traverse the interplanar gap, resulting in a collision with the atoms of a neighboring plane. Because little resistance to atomic motion exists within the interplanar gap, PKAs entering the gap are capable of traveling a long distance relative to the interatomic spacing of the system. Therefore, such PKAs generally reach an equilibrium position far from their original lattice sites, making recombination an unlikely scenario.

The calculated, θ-averaged E_d values of Fig. 5-18 (labeled as "NCSU arithmetic mean") accord fairly well with the measurements of Montet and Iwata and usually fall between their respective curves. At 300 K and 700 K, however, the computed E_d at $\Phi=0°$ lies significantly above the corresponding data reported by Iwata and Montet. This phenomenon is believed to arise from the fact that a PKA oriented along $\Phi=0°$ enters into the cutoff range of neighboring atoms (both above and below) after moving a distance of only 1 Å. The PKA then experiences a force which, due to symmetry, points directly back towards its initial position. Contrastingly, intermediate knock-on angles cause the PKA to enter an undamaged region where the symmetry of its surroundings locks it approximately halfway between neighboring planes. Hence, recombination is more probable at $\Phi = 0°$, resulting a larger apparent E_d.

Chapter 6

Conclusions and Future Work

6.1 Conclusions

Molecular dynamics techniques have been implemented to study the physical properties of graphite at temperatures spanning 0 K – 1800 K. These studies entailed the development of a graphite-specific MD code based on the 2nd generation REBO potential for hydrocarbons, with modifications introduced as needed to fit high temperature experimental data such as mean squared displacement and thermal expansion. The adjustments to the REBO potential include a plane-by-plane center of mass velocity correction, a supplementary cutoff term representing long-range forces, and temperature-dependent adjustments to the pairwise attractive and repulsive coefficients. Each adjustment to the potential function was parameterized to fit a specific physical property throughout the investigated range of temperatures.

The NCSU MD code, containing the modified REBO potential, was shown to accurately compute thermal expansion and out-of-plane MSD up to 1800 K. Furthermore, the high temperature behavior of other properties such as average potential energy and mean interatomic distance was demonstrated to be physically sound. As a theoretical test case, the standard deviation in temperature was calculated in the microcanonical ensemble and compared to its corresponding statistical mechanical prediction. The MD results exhibited very good agreement with the theoretical model.

The NCSU MD code was subsequently utilized to calculate the threshold displacement energy of graphite from room temperature to 1800 K. The full range of non-

equivalent knock-on angles and lattice sites was considered, and a total of 28 individual E_d measurements were performed at each temperature. It was discovered that the computed E_d generally increases as the in-plane component of the simulated knock-on event becomes dominant. This observation was explained on the basis of the layered structure of graphite. Furthermore, threshold displacement calculations (averaged over the polar angle) were found to accord well with the conclusions of two electron irradiation studies reported in literature.

6.2 Future Work

6.2.1 Cascade Collisions

The threshold displacement study performed in this work could be augmented by examining the keV-range PKAs that would be expected to arise in a graphite moderator. At these energies, the PKA would be capable of dislodging many other carbon atoms through collision cascades, and the formation of defect clusters would therefore become feasible. The damaged structure that results from such simulations could then be used to infer the properties of an irradiated graphite moderator.

However, a few changes to the MD code would be necessary in order to accommodate high energy PKAs. For example, larger supercells would likely be required as the damaged region increases in extent. Also, if the layered structured of graphite is subjected to significant local deformation (as would be expected from a high energy PKA), the out-of-plane cutoff function may no longer act as a good approximation to the true long range forces. In this situation, an explicit calculation of long range forces may be needed, at least in the vicinity of a deformation.

6.2.2 Nuclear Grade Graphite

The next phase of this work is to devise and implement a methodology for modeling nuclear-grade graphite, which is a two-phase mixture of pyrolytic carbon and amorphous binder carbon. Unlike pure pyrolytic graphite, nuclear-grade graphite also contains a pore structure that lowers its average density. Due to the lack of microscopic uniformity in nuclear graphite, modeling efforts will need to be expanded to account for the coexistence of multiple microstructures.

Because nuclear graphite is the preferred form of graphite for application in power reactors, its thermal neutron scattering cross sections are of particular interest. The procedure outlined in section 1.3 could be utilized to compute the scattering cross section from atomic trajectory data. The effects of irradiation could also be examined by first evolving a damaged graphite structure from high energy cascade collisions, as described in the previous section. Results derived from these simulations would be highly useful in predicting how the accumulation of radiation damage affects the thermal flux spectrum of the reactor core.

References

[1] *A Technology Roadmap for Generation IV Nuclear Energy Systems.* December 2002. *US. DOE and Generation IV International Forum.* July 2007. < http://nuclear.inl.gov/gen4/docs/gen_iv_roadmap.pdf>

[2] B. T. Kelly, B. J. Marsden and K. Hall. *Irradiation Damage in Graphite due to Fast Neutrons in Fission and Fusion Systems* TECDOC-1154. International Atomic Energy Agency, Vienna, Austria, (2000). Available online at http://www.iaea.org.

[3] A. I. Hawari, I. I. Al-Qasir and A. M. Ougouag. *Nuc. Sci. & Eng.*, **155**, 449 (2007).

[4] A. I. Hawari, I. I. Al-Qasir, V. H. Gillette, B. W. Wehring and T. Zhou. "*Ab Initio* Generation of Thermal Neutron Scattering Cross Sections." PHYSOR 2004, Chicago, Illinois, April 25-29 (2004).

[5] *Molecular Dynamics Simulations: CHARMM Tutorial.* R. Stote, A. Dejaegere, and D. Kuznetsov. 26 October 1999. *European Molecular Biology Network.* April 2007. <http://www.ch.embnet.org/MD_tutorial/>

[6] M. P. Allen. *Computer Simulation of Liquids.* Oxford University Press, Oxford, UK, (1987)

[7] C. W. Gear. *Numerical Initial Value Problems in Ordinary Differential Equations.* Prentice-Hall, Englewood Cliffs, NJ (1971).

[8] D. L. G. Cheung. *Structures and Properties of Liquid Crystals and Related Molecules from Computer Simulation.* Diss. University of Durham, (2002). Durham, UK. < http://cmt.dur.ac.uk/sjc/thesis_dlc/node5.html >

[9] J. Tersoff. *Phys. Rev. Lett.*, **39**, 5566 (1989).

[10] G. C. Abell. *Phys. Rev. B.*, **31**, 6184 (1985).

[11] D. W. Brenner. *Phys. Rev. B.*, **42**, 9458 (1990).

[12] D. W. Brenner, O. A. Shenderova, J. A. Harrison, S. J. Stuart, B. Ni, and S. B. Sinnott, *J. Phys.: Cond. Matt.*, **14**, 783 (2002).

[13] S. J. Stuart, A. B. Tutein, and J. A. Harrison. *J. Chem. Phys.*, **112**, 6472 (2000).

[14] B. T. Kelly, *Physics of Graphite*, Applied Science Publishers LTD, UK, 200 (1981).

[15] B. D. Hehr, A. I. Hawari, and V. H. Gillette. "High Temperature Graphite Simulations using Molecular Dynamics," to be published in *Transactions of the American Nuclear Society*, June / July (2007).

[16] C. Kittel, *Introduction to Solid State Physics*, Wiley, New Jersey, USA, 58 (2005).

[17] D. Frenkel, and B. Smit, *Understanding Molecular Simulation: From Algorithms to Applications*, Academic Press, San Diego, (2002).

[18] B. D. Hehr, A. I. Hawari, V. H. Gillette, and A. M. Ougouag. *Transactions of the American Nuclear Society.* **95**, 952 (2006).

[19] B. H. Billings and D. E. Gray, *American Institute of Physics Handbook*, McGraw-Hill, New York (1972).

[20] E. G. Steward, B. P. Cook, and E. A. Kellet, *Nature*. **187**, 1015 (1960).

[21] A. C. Bailey and B. Yates, *J. Appl. Phys*., **41**, 5088 (1970).

[22] S. Yip. 2006. *Introduction to Modeling and Simulation: Diffusion at the Particle Level*. Cambridge: Massachusetts Institute of Technology. [Course notes.]

[23] E. Fitzer and U. Funk. *Carbon*. **16,** 85 (1978).

[24] B. Firey, F. W. de Wette, and E. de Rouffignac, *Phys. Rev. B*, **28**, 7210 (1983).

[25] B. T. Kelly, *Journal of Nuclear Materials*, **24**, 210 (1967).

[26] E. A. Kellett, B. P. Jackets and B. P. Richards. *Carbon*, **2**, 175 (1964).

[27] B. Post, Crystall. Conf. at Cambridge (1960).

[28] M. Hasegawa and K. Nishidate, *Phys. Rev. B*, **70,** 205431 (2004).

[29] G. L. Montet, *Carbon*, **5**, 19 (1967).

[30] T. Iwata and T. Nihira, *Phys. Lett.,* **23**, 631 (1966).

[31] K. Huang, *Statistical Mechanics,* Wiley, New York, USA, (1987).

[32] D. S. Corti. *Phys. Rev. E,* **64**, 016128 (2001).

[33] F. Ercolessi. *A Molecular Dynamics Primer*, University of Udine, (1997). Udine, Italy. < http://www.fisica.uniud.it/~ercolessi >

[34] M. Tuckerman. 2001. *Energy Fluctuations in the Canonical Ensemble.* New York: New York University. [Course notes].

Appendix

Appendix A

Statistical Ensemble Theory

Introduction

The purpose of this appendix is to provide the interested reader with a more detailed description of the aspects of statistical mechanics that are relevant to computational MD.

The concept of particle ensembles arises frequently in statistical mechanics and constitutes the theoretical basis for the behavior of any molecular dynamics system. In general, the term "ensemble" refers to the (possibly infinite) microscopic configurations of a system commensurate with a given set of macroscopic constraints on such quantities as temperature, volume, particle number, chemical potential, or total energy.

The majority of MD simulations are performed using an NVE (constant number-volume-energy), NVT (constant number-volume-temperature), or NPT (constant number-pressure-temperature) ensemble. While all real systems, in principle, obey the constraint of constant total energy, ensembles other than NVE are often desirable depending on the purpose of the simulation. For example, experiments are normally performed under conditions of constant temperature and pressure – readily measurable macroscopic quantities that may be controlled and reproduced with ease. In contrast, the total energy or number of particles cannot be directly measured.

Thus, it would appear that the preferred ensemble (in terms of replicating laboratory conditions) would fix easily measurable thermodynamic quantities. Fundamental to statistical mechanical theory, however, is the principle that all ensembles must equivalently

predict the observables of the system in the thermodynamic limit (i.e. as the number of particles approaches Avogadro's number).

General Concepts

In this section, the relevant concepts and nomenclature of statistical mechanics are introduced. The material presented here is foundational to the discussion of ensemble theory that follows. Throughout the remainder of this discussion, the *postulate of equal a-priori probabilities* will be assumed, which states that [31]:

> *When a macroscopic system is in thermodynamic equilibrium, it is equally likely to be in any state satisfying the macroscopic conditions of the system.*

In practice, this key postulate is virtually required to derive any useful result from statistical mechanics. The numerous successes of statistical mechanical theory serve as justification for the *postulate of equal a-priori probabilities*.

Phase Space and Entropy

Phase space is the space that encompasses all possible states of the system, with each point in phase space corresponding to a unique state. For every degree of freedom, there exists a corresponding axis in phase space. Therefore, in a classical system of *N* particles with 3N coordinate components (q_1, q_2, …, q_{3N}) and 3N momentum components (p_1, p_2 , …, p_{3N}), there will be a total of 6N mutually orthogonal axes.

The probability density of finding the system in a state $(\vec{q}, \vec{p})$ about $dq^{3N} dp^{3N}$ is designated by $\rho(\vec{q}, \vec{p})$. So,

$\rho(\vec{q}, \vec{p}) d^{3N} q d^{3N} p$ = number of representative points contained in $dq^{3N} dp^{3N}$

The volume occupied by a system in phase space is:

$$\Gamma(E, N, V) = \int d^{3N} q d^{3N} p \tag{A.1}$$

where the integral extends over all allowed values of q and p. The microscopic definition of entropy follows from the above equation and may be written as:

$$S(E, N, V) = k_B \ln \Gamma(E, N, V) \tag{A.2}$$

where k_B is Boltzmann's constant.

Thermodynamic Potentials

Three thermodynamic potential functions are commonly used to characterize the state of the system. These are the enthalpy:

$$H = U + PV \tag{A.3}$$

The Helmholtz free energy:

$$A = U - TS \tag{A.4}$$

And the Gibbs free energy:

$$G = U + PV - TS \tag{A.5}$$

where U refers to internal energy. The latter two functions are significant because they establish the equilibrium state of a system that is not totally isolated from its environment. Specifically, if a system is mechanically isolated and at constant temperature, its Helmholtz

free energy never decreases. Therefore, the equilibrium state of the system corresponds to the state of minimum Helmholtz free energy. Similarly, the Gibbs free energy of a system at constant temperature and pressure cannot decrease, implying that the equilibrium state is the state of minimum Gibbs free energy [31].

Observables

The probability density function, $\rho(\vec{q}, \vec{p})$, provides the necessary connection between the microscopic attributes and macroscopic observables of the system. Expressly, equilibrium averages can be computed as weighted phase space integrals of the form:

$$\langle \vartheta \rangle = \frac{\int \vartheta(\vec{q}, \vec{p}) \rho(\vec{q}, \vec{p}) d^{3N} q \; d^{3N} p}{\int \rho(\vec{q}, \vec{p}) d^{3N} q \; d^{3N} p} \tag{A.6}$$

where ϑ is some quantity of interest. This expression should be interpreted as an average over all possible microscopic configurations of the system, weighted by the relative probability of each configuration. The denominator of Eq. (A.6) is often referred to as the *partition function*:

$$Z = \int \rho(\vec{q}, \vec{p}) d^{3N} q \; d^{3N} p \tag{A.7}$$

which may be evaluated once $\rho(\vec{q}, \vec{p})$ is specified. Most thermodynamic quantities may be directly computed from the partition function; therefore, the primary task is to determine $\rho(\vec{q}, \vec{p})$ for the system of interest.

Ergodic Hypothesis

Under experimental conditions, system observables are usually measured as time averages rather than ensemble averages. Because these two averaging techniques are distinct, their equivalence is not immediately obvious. The validity of Eq. (A.6) lies in the so-called *Ergodic hypothesis*, which states that the ensemble average over an equilibrated system is identical to the time average assuming that the sampling time is sufficiently long. In other words, given enough time, the state of the system will pass arbitrarily close to every representative point in its phase space.

Ensembles

The ensembles most commonly utilized in MD will now be described. Subsequently, their connectedness in the thermodynamics limit will be demonstrated.

Microcanonical (NVE) Ensemble

The microcanonical ensemble corresponds to a system with constant volume, particle number, and total energy. More exactly, the energy is constrained to lie between E and E + Δ, where Δ << E. The occupied volume of phase space is then:

$$\Gamma(E) = \int_{E<H(\vec{q},\vec{p})<E+\Delta} d^{3N}q \; d^{3N}p \tag{A.8}$$

which is represented geometrically as a spherical shell of inner radius $\sqrt{2mE}$ and outer radius $\sqrt{2m(E+\Delta)}$. The density of states, defined as the number of states per unit energy about E, is given by:

$$w(E) = \frac{\Gamma(E)}{\Delta} \tag{A.9}$$

Using Eq. (A.2) for the entropy, the temperature and pressure may be calculated from the following relations:

$$T = \left(\frac{\partial E}{\partial S}\right)_V \tag{A.10}$$

$$P = -\left(\frac{\partial E}{\partial V}\right)_S \tag{A.11}$$

from which the equilibrium properties of the system are derivable.

The microcanonical ensemble is the simplest to implement in an MD program. In a typical microcanonical simulation, periodic boundary conditions maintain a constant volume, while the number of particles scales with the supercell size (an input parameter) and conservation of energy is assured by the smoothness and time invariance of the potential function (neglecting possible error from the numerical integration scheme).

Canonical (NVT) Ensemble

The canonical ensemble corresponds to a system with constant volume, particle number, and temperature. System temperature is maintained through contact with a thermal bath. Under these conditions, it can be shown that:

$$\rho(\vec{q}, \vec{p}) \propto \exp\left[\frac{-H(\vec{q}, \vec{p})}{kT}\right] \tag{A.12}$$

and the partition function takes the form:

$$Z(V,T) = \int \frac{d^{3N}q \; d^{3N}p}{N!h^{3N}} \exp\left[-\beta H(\vec{q}, \vec{p})\right] = \exp\left[-\beta A(V,T)\right] \tag{A.13}$$

where $\beta = 1/(k_B T)$ and h is Plank's constant. Integration is performed over the totality of phase space. For the canonical ensemble, Helmholtz free energy is the thermodynamic function of choice because it is minimized in a constant temperature system. In terms of the partition function, the Helmholtz free energy may be written as:

$$A(N,V,T) = -k_B T \log Z \tag{A.14}$$

from which the pressure, entropy, and internal energy can be computed as:

$$P = -\left(\frac{\partial A}{\partial V}\right)_{N,T} \tag{A.15}$$

$$S = -\left(\frac{\partial A}{\partial T}\right)_{N,V} \tag{A.16}$$

$$U = -\left(\frac{\partial \ln Z}{\partial \beta}\right)_{N,V} = A + TS \tag{A.17}$$

In an MD program, the particle velocities must be manipulated in some manner to maintain constant temperature. A few of the more widely used schemes are described below.

- ***Velocity rescaling*** – All particle velocities are scaled by a common factor to attain the desired temperature (see section 2.8). While simple, this method continually perturbs the system.
- ***Thermal bath*** – Velocities are rescaled only in some user-defined "bath" region of the supercell. This is the approach taken in the present work and has the advantage of leaving most atoms unperturbed.
- ***Nose-Hoover Thermostat*** – An extra degree of freedom is introduced into the Hamiltonian, thereby altering the equations of motion. The added degree of freedom is designed to generate the probability density given in Eq. (A.12).

Isobaric Isothermal (NPT) Ensemble

The isobaric isothermal ensemble corresponds to a system with constant volume, particle number, and pressure. In the thermodynamic limit, it can be shown that the partition function for this ensemble is [32]:

$$Z = \frac{P}{kT}\int \exp\left[-\beta A(N,V,T)\right]\cdot \exp\left[\frac{-PV}{kT}\right]dV \tag{A.18}$$

Analogously to the canonical ensemble, the characteristic state function is the Gibbs free energy which may be expressed as:

$$G = -kT\ln Z \tag{A.19}$$

which links to other state functions through Eq. (A.5).

Implementing the NPT ensemble in MD necessitates computation of the system pressure from atomistic-level data. The pertinent relation is called the *virial equation* and is given by [33]:

$$PV = NkT + \frac{1}{D}\left\langle \sum_{i=1}^{N} \vec{r}_i \cdot \vec{F}_i \right\rangle \tag{A.20}$$

where $\vec{r}_i$ is the position vector of atom i, $\vec{F}_i$ is the force acting on atom i due to interatomic interaction, and D is the dimensionality of the system (usually 2 or 3). Two schemes for controlling the pressure are mentioned below.

- ***Berensden method*** – The supercell is coupled to a "pressure bath" which maintains the correct time-averaged pressure through scaling of the system volume
- ***Melchionna method –*** A Nose-Hoover type barostat is integrated directly into the equations of motion. The barostat is designed to generate the correct ensemble-averaged pressure.

Ensemble Fluctuations

Each ensemble allows certain properties to fluctuate while others are held invariant. The canonical ensemble, for instance, places no constraint on particle energy as long as the temperature is constant, and the microcanonical ensemble places no restriction on temperature as long as the total energy is fixed. Among those properties that are permitted to vary, the degree of fluctuation will now be examined in more detail. It will be shown that, in the thermodynamic limit, deviations from the most probable value are so small that the various ensembles are practically equivalent.

As an example, the standard deviation of energy in the canonical ensemble will be calculated. From Eq (A.17):

$$E = \langle H \rangle = -\frac{\partial}{\partial \beta} \ln Z \tag{A.21}$$

$$\langle H \rangle^2 = \left(\frac{\partial}{\partial \beta} \ln Z \right)^2 \tag{A.22}$$

and the mean of the squared Hamiltonian is [34]:

$$\langle H^2 \rangle = \frac{\int dqdp H^2(q,p) \exp[-\beta H(q,p)]}{Z} \tag{A.23}$$

$$= \frac{\int dqdp \frac{\partial^2}{\partial \beta^2} \exp[-\beta H(q,p)]}{Z}$$

$$= \frac{1}{Z} \frac{\partial^2}{\partial \beta^2} Z$$

$$= \frac{\partial^2}{\partial \beta^2} \ln Z + \left[\frac{1}{Z} \frac{\partial Z}{\partial \beta} \right]^2$$

$$\left\langle H^2 \right\rangle = \frac{\partial^2}{\partial \beta^2} \ln Z + \left[\frac{\partial}{\partial \beta} \ln Z \right]^2 \tag{A.24}$$

Therefore, the standard deviation in energy is:

$$\sigma_E = \sqrt{\left\langle H^2 \right\rangle - \left\langle H \right\rangle^2} = \sqrt{\frac{\partial^2}{\partial \beta^2} \ln Z} \tag{A.25}$$

But from Eqs. (A.13) and (A.17),

$$\frac{\partial^2}{\partial \beta^2} \ln Z = kT^2 \left(\frac{\partial E}{\partial T} \right)_V = kT^2 C_v \tag{A.26}$$

where C_v is the heat capacity at constant volume. The standard deviation in energy can now be expressed as:

$$\sigma_E = \sqrt{kT^2 C_v} \tag{A.27}$$

and the fractional deviation is given by:

$$\frac{\sigma_E}{E} = \frac{\sqrt{kT^2 C_v}}{E} \tag{A.28}$$

Noting that $C_v \propto N$, $E \propto N$, and T = constant, the following relation becomes evident:

$$\frac{\sigma_E}{E} \propto \frac{\sqrt{kT^2 N}}{N} \propto \frac{1}{\sqrt{N}} \tag{A.29}$$

which indicates that energy fluctuations in the canonical ensemble are normally distributed about the mean energy, $\langle E \rangle$. In the thermodynamic limit ($N \to 10^{23}$), the peak at $\langle E \rangle$ is extremely sharp, and for all practical purposes the energy is constant at $\langle E \rangle$. Consequently, $\sigma_E \to 0$ as $N \to \infty$ and the canonical ensemble becomes equivalent to the microcanonical ensemble.

The analogous example of temperature deviation in the microcanonical ensemble was detailed in section 5.2.2. In that case, it was similarly demonstrated that temperature fluctuations assume a normal distribution about the mean. This type of distribution, in fact, is a general result for ensemble state variables and serves to link the various ensembles at the macroscopic level.

Significantly, the number of particles in a typical MD simulation falls short of the thermodynamic limit by many orders of magnitude, leading to observable (though generally small) deviations in the state variables. Because of this difference in scale, the choice of ensemble exerts a noticeable impact on MD results.

Appendix B

Parallelization

Cell Structure

To facilitate the investigation of large systems (on the order of 10^4 to 10^6 atoms), the NCSU MD code was endowed with parallel processing capability. The parallelization is implemented by dividing the supercell into a mesh of LxMxN nodes, where

$$\#\ processors = (L)(M)(N)$$

The volume assigned to each node is uniform, though the spacing of the mesh along the x,y, and z axes need not be of equal width. Each node is further divided into a grid of "link cells", the dimensions of which are specified by the user. An example of a parallelized 2D supercell is given in Fig. B-1.

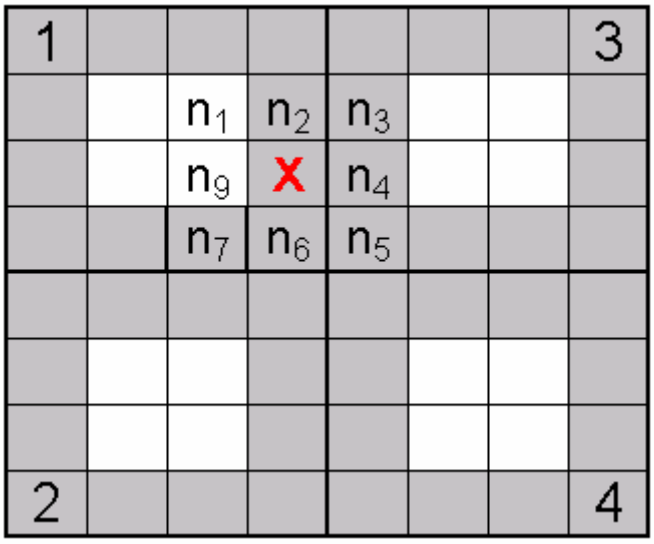

Fig. B-1. Schematic of a two dimensional parallelized supercell

Heavy black lines mark the borders of the nodes (labeled 1,2,3, and 4) while thin black lines delimit the individual link cells. The four cells at the center of each node are the *core cells*, and the shaded cells along the periphery are the *skin cells*.

The purpose of the link cell structure is to increase the efficiency of interatomic force calculations. To illustrate this point, node 1 of Fig. B-1 shall now be examined in detail. During the force calculation phase of the MD code, each of the 16 link cells contained within node 1 is evaluated sequentially. For each atom in the evaluated cell, the range of possible interaction is bounded by a square of 3x3 cells centered on the evaluated cell (i.e. the atoms of all neighboring cells plus the evaluated cell are considered as candidates for interaction). The distance is then computed between each atom in the evaluated cell and all other candidate atoms. If any interatomic distance is found to be less than the potential energy cutoff distance, an interaction is scored and force calculations are performed. Under this scheme, the efficiency of the program is maximized by minimizing the link cell volume (and hence, the number of candidate atoms), subject to the constraint that the volume must be sufficiently large to account for all interacting pairs.

For all *core cells*, the range of possible interaction falls solely within the volume assigned to the mother node. *Skin cells*, on the other hand, are partially bordered by the cells of other nodes. For example, among the neighbors $n_1 - n_9$ of the cell marked by the red "x" in Fig. B-1, cells n_3, n_4, and n_5 are assigned to node 3. In this situation, some degree of internodal communication is required to identify all candidates for interaction. The program handles this by storing the atomic positions of cells n_3, n_4, and n_5 within the database of node 1. To generalize, each node stores the updated atomic positions of all *skin cells* that are in

contact with its boundary. Should any atom depart from the volume of its node of residence, it is sent to the appropriate neighbor node.

Parallel Efficiency

In contrast with, e.g., the *Monte Carlo* method, molecular dynamics simulations must proceed in a deterministic manner such that different time steps cannot be run in parallel (as would otherwise be the most efficient scenario). Consequently, the aforementioned geometry splitting scheme is the most viable parallelization technique in spite of efficiency losses arising from internodal communication. Tasks requiring such communication include:

- Maintaining updated lists of atomic data in the *skin cells*
- Transferring atoms that cross an internodal boundary
- Calculating global quantities of interest (such as the average potential energy, the temperature, the center of mass velocity, and the mean squared displacement).

Assuming that the number of atoms assigned to each node is sufficiently large (on the order of 10^4) and the range of interaction is relatively short, the computational cost of internodal communication will be much less than the cost of evaluating interatomic forces, and the time required for completion of the simulation will exhibit nearly linear behavior with respect to the number of processors. Thus, in terms of both efficiency and memory storage, parallelization in MD is particularly well suited for simulations involving a very large system subject to short-ranged forces.